University of Stuttgart
Germany

Water Level Monitoring at SAPOS Stations through GNSS-IR - a case Study at the Station Iffezheim

Sven B. Wagner

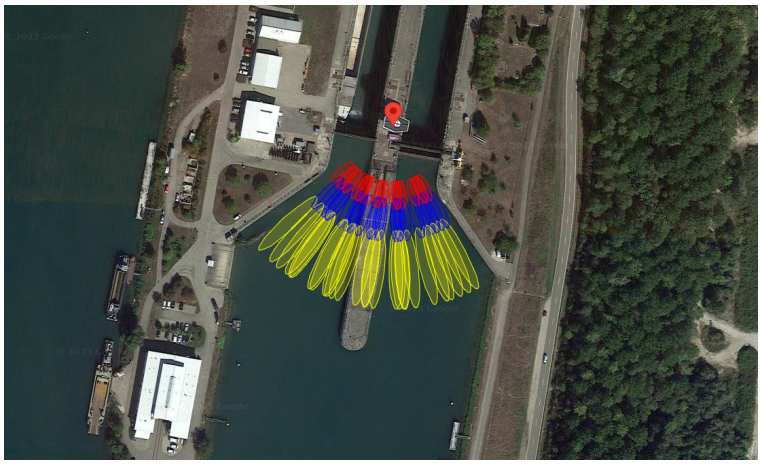

Bachelor thesis

in the degree program Geodäsie und Geoinformatik

Institute of Geodesy, University of Stuttgart

Stuttgart, December 2023

Supervisor: Prof. Dr.-Ing. Nico Sneeuw
Universität Stuttgart

Dr.-Ing. Mohammad Tourian
Universität Stuttgart

GIS

Erklärung der Urheberschaft

Ich erkläre hiermit an Eides statt, dass ich die vorliegende Arbeit ohne Hilfe Dritter und ohne Benutzung anderer als der angegebenen Hilfsmittel angefertigt habe; die aus fremden Quellen direkt oder indirekt übernommenen Gedanken sind als solche kenntlich gemacht. Die Arbeit wurde bisher in gleicher oder ähnlicher Form in keiner anderen Prüfungsbehörde der Universität Stuttgart oder einer anderen Hochschule vorgelegt, und auch noch nicht veröffentlicht.

Date

Signature

Declaration of authorship

I declare in lieu of an oath, that the research reported within this thesis has been conducted by the author unless indicated otherwise. Ideas provided directly or indirectly by others have been marked for that. The material contained within this thesis has not previously been submitted for a degree to the examination authority of the University of Stuttgart or any other University, and is also not published otherwise.

Acknowledgements

I would first like to thank my supervisor, Prof. Dr.-Ing. Nico Sneeuw, from the Institute of Geodesy at the University of Stuttgart. Prof. Sneeuw supported me with wealth of knowledge and a constant willingness to assist with my queries and challenges. His guidance was instrumental in shaping this thesis and allowed me the autonomy to develop and present my research as intended.

I would also like to thank the dedicated members of the Institute, including Dr.-Ing. Mohammad Tourian, whose insightful comments and assistance enriched this work and Dipl.-Ing. (FH) Ron Schlesinger for his technical support and guidance, as well as his role in organising data acquisition.

I take this opportunity to also thank the LGL for generously providing the crucial data that forms the foundation of this thesis. My thanks extend to Denis Kleinecke for facilitating the smooth transfer of data.

I also place on record my very profound gratitude to Prof. Kristine Larson whose significant contributions to the field of GNSS-Interferometric-Reflectometry greatly influenced this thesis. Her continuous efforts, insightful studies, and the GNSS-IR software package used in this research have been invaluable.

Abstract

The German SAPOS-Network comprises approximately 270 permanent GNSS receivers, capturing signals from Global Navigation Satellite Systems such as GPS, GLONASS, Galileo, and BeiDou. Primarily employed for generating kinematic, mathematical, and physical models within their respective regions, these receivers hold untapped potential for alternative applications.

GNSS receivers capture multipath errors, typically considered unwanted interferences resulting from signal reflections off surfaces beneath the antenna. Despite their potential to adversely affect data precision, these interferences contain valuable information about the reflecting surface. As satellites pass through the receivers' field of view at specific elevation angles, the interference between the direct and reflected signals leads to constructive and destructive patterns. This phenomenon occurs due to variations in signal phase between the direct and reflected signal, enhancing or dampening the signal strength.

These variations in signal strength are captured in the satellites Signal-to-Noise Ratio (SNR) data. Spectral analysis of the SNR data can be used to determine the frequency of the interference pattern. Combining this frequency with the corresponding signal wavelength and satellite elevation angles allows the calculation of the vertical distance between the antenna phase centre and the reflecting surface on Earth. This method, known as GNSS Interferometric Reflectometry (GNSS-IR), provides a valuable means of monitoring surface information, including soil moisture, snow depth, and water levels.

At SAPOS stations near rivers and water bodies, GNSS-IR offers a cost-effective, accessible, and innovative opportunity to gather water level information using the already existing infrastructure. This research explores the potential of GNSS-IR for water level monitoring at SAPOS stations focusing on the Iffezheim station along the Rhine River near the City of Karlsruhe in southern Germany.

Contents

List of Figures

1. Introduction

"GNSS-Interferometric-Reflectometry is a technique that uses data from (geodetic-quality) GNSS instruments for sensing the near-field environment" (Roesler & Larson, 2018).

The Global Navigation Satellite System (GNSS) is the collection of several global satellite systems such as the NAVSTAR GPS (Global Positioning System) of the United States of America, GLONASS (Global Satellite Navigation System/Globalnaja nawigazionnaja sputnikowaja sistema) of the Russian federation, Galileo of the European Union and BeiDou of the Peoples Republic of China. Originally used to precisely navigate the United States' armed forces in the mid-1970s, the Global Positioning System quickly became a system-of-opportunity for a wide range of scientific applications. Today, GNSS stands as an invaluable resource, providing precise positioning and temporal data for applications such as navigation, surveying, geodesy, timing synchronisation, and remote sensing, contributing significantly to scientific and societal advancements. Each GNSS system comprises a constellation of 24 to 32 satellites in medium Earth orbit, with satellites rising and setting in the sky multiple times per day (Langley et al., 2017). The technology involves measuring the distance between a receiver and satellites using pseudorange, carrier phase, and Doppler measurements. The distance between a GNSS satellite and a receiver is derived from the time it takes for the signal to propagate from the satellite to the receiver. The basic measurement made by a GNSS receiver is the time τ required for the GNSS signal to travel from the satellite to the receiver. Since the signal travels at the speed of light c, the time interval can be converted to a distance or range by multiplying it by the speed of light. The pseudorange r can be calculated using the formula:

$$r = c \cdot \tau \tag{1.1}$$

This formula assumes ideal conditions where the receiver and satellite clocks are synchronised, and there are no atmospheric delays or measurement noise. However, in reality, there are clock errors and atmospheric delays that need to be accounted for in the calculations, therefore it is called pseudo-range. To accurately determine the receiver's position, the receiver needs to measure the pseudo-ranges to at least four satellites simultaneously. By receiving signals

from at least four satellites, the receiver can perform trilateration calculations to determine its position. Trilateration involves intersecting spheres or circles centred around each satellite with radii equal to the measured distances. The point where the spheres intersect represents the receiver's position (Langley et al., 2017). GNSS has become an enabling technology for new applications such as location-based services, precision agriculture, machine control and the development of scientific studies like GNSS-Interferometric-Reflectometry (GNSS-IR).

1.1. Keywords

1.1.1. Reflectometry and Interferometry

Reflectometry

The term reflectometry involves utilising the reflection of waves or pulses at surfaces and interfaces to detect or characterise objects. In the context of GNSS-IR, this concept manifests through the examination of satellite signal reflections on a designated surface, such as the Rhine River. By analysing the Signal-to-Noise Ratio (SNR) data and the corresponding interference pattern of the reflected signals, the height of the reflector above the water surface can be derived.

Interferometry

Interferometry, on the other hand, is a technique that extracts information by leveraging the interference of superimposed waves. In GNSS-IR, this technique is applied to analyse the interference patterns created by the interaction between direct and reflected satellite signals. By analysing the SNR data the frequency of the interference pattern can be determined, which combined with the corresponding signal wavelength and satellite elevation angles enables the calculation of the vertical distance between the GNSS antenna phase centre and the reflecting surface on the Earth.

1.1.2. Nyquist Frequency and Lomb-Scargle-Periodogram

Nyquist-Shannon Sampling Theorem

The Nyquist-Shannon sampling theorem establishes a fundamental principle in signal processing. It states that the sampling rate required to accurately reproduce a signal must be at least twice the frequency of its highest component, otherwise the signal is undersampled. Undersampling results in spectral distortion known as aliasing. The initial frequency at which aliasing occurs is referred to as the Nyquist-Frequency. Conversely, if the signal contains only frequencies lower than the Nyquist frequency, it is oversampled.(Por et al., 2019).

The Lomb-Scargle-Periodogram

The Lomb-Scargle-Periodogram (LSP) (Lomb, 1976; Scargle, 1982) extends the principles of the Fourier Transformation to analyse periodic signals and identify dominant frequencies within unevenly sampled data. According to VanderPlas (2018), the periodogram is constructed by fitting a sinusoidal model to the data at each frequency, followed by computing the power of the residuals of the fit. The frequency with the highest power in the periodogram is considered the estimated frequency of the periodic signal. The amplitude and phase of the sinusoidal model at that frequency can be used to characterise the signal. As emphasised by VanderPlas (2018), it is crucial to consider some practical aspects when using the LSP to analyse data. This involves choosing an appropriate frequency grid, where both the frequency limit and the grid spacing require careful consideration, as well as a cautious choice of normalisation and the treatment of outliers in the data.

1.1.3. Fresnel Zones

A fundamental principle in wave propagation is the concept of the Fresnel zones. First introduced by Fresnel in 1818 to explain diffraction phenomena using Huygens' principle, the Fresnel zone, as described by Pearce and Mittleman (2002) defines the area where the reflections of a wave-incident on a reflecting target contribute to a coherent sum of disturbance received by a detector. Traditionally, the first Fresnel zone is defined as the largest reflecting disk for which all reflected waves reach the detector with phase shifts $\Delta\phi \leq \pi$ (Pearce & Mittleman, 2002). In the context of GNSS-IR, the Fresnel zone, often referred to

as the reflection zone, specifies the area on the reflecting surface where reflected signals can be leveraged to compute reflector heights, due to the interference derived from the Signal-to-Noise ratio data.

1.1.4. Tropospheric and Ionospheric Delay

The troposphere and ionosphere, integral components of the Earth's atmosphere, exert significant influence on the propagation of signals in Global Navigation Satellite Systems, deriving from the refractive index of the constituent gases. Understanding the delays induced by signal traversal through these atmospheric layers is imperative for accurate GNSS applications.

Ionospheric delay

The ionosphere, spanning from approximately 60 km to over 1000 km in height, contains a partially ionised medium generated by solar radiation and charged particles. The propagation speed of GNSS electromagnetic signals within the ionosphere is proportional to the total electron content (TEC) along the path from the transmitter to the receiver (Klobuchar, 1983). The TEC and, consequently, the ionospheric refraction depend on the location of the receiver, the hour of the day, and solar activity. As the ionosphere is a dispersive medium, meaning wave propagation speed and refractive index depend on frequency, employing dual-frequency measurements can mitigate more than 99.9 % of the ionospheric delay (first order ionospheric effects). Single-frequency receivers necessitate the application of ionospheric prediction models for mitigation (J. Sanz Subirana & Hernández-Pajares, 2011a).

Tropospheric delay

Beneath the ionosphere lies the troposphere, extending from the Earth's surface to an altitude of approximately 10 to 12 km. In GNSS terms, the troposphere often encompasses the tropopause and stratosphere up to 50 km, then referring to the whole neutral atmosphere. The troposphere induces a time delay on electromagnetic signals, which is not frequency-dependent and therefore cannot be eliminated by dual-frequency measurements as is done for ionospheric effects. The tropospheric delay arises from a hydrostatic component, caused by dry gases such as nitrogen, oxygen and argon, which make up more than 99.9 % of the dry air mass. This component varies with temperature and pressure and

is quite predictable. There is also a wet component caused by water vapour and condensed water, which is challenging to model due to its arbitrary nature. The tropospheric delay is modelled in zenith direction and depends on the signal path through the neutral atmosphere. It can be projected into the direction of the satellite using a mapping function of satellite elevation angle (and several atmospheric parameters) (Schüler, 2001). For example, Collins (2001) presented a tropospheric model where a common mapping function for the zenith wet delay (ZWD) and zenith hydrostatic delay (ZHD) is used. This leads to:

$$T(e) = (ZWD + ZHD) \cdot M(e) \tag{1.2}$$

where ZWD and ZHD are dependent on meteorological parameters, as well as the latitude and height of the antenna. The zenith hydrostatic delay typically accounts for 95 % of the total zenith delay. $M(e)$ represents the mapping function after Black and Eisner (1984), according to J. Sanz Subirana and Hernández-Pajares (2011b):

$$M(e) = \frac{1.001}{\sqrt{(0.002001 + \sin^2 e}} \tag{1.3}$$

which is valid for satellite elevation angles e over 5 °. The tropospheric delay directly affects GNSS-IR, leading to a shift in the estimated reflector height and altering the oscillation frequency. For small sites, tropospheric delay may be negligible, but for sites above 10 m, it must be considered and corrected. Williams (2023) suggests correcting for tropospheric delay by stretching elevation angles before calculating the Lomb-Scargle-Periodogram (LSP). He furthermore states that, for instance, at a site 17 m above water, the tropospheric delay reaches a median value of 11.5 cm, underscoring the significance in precise GNSS-IR applications.

1.1.5. Inter-Frequency Bias

In the realm of GNSS processing, the estimated position is intricately linked to the antenna phase centre, a non-physical point that exhibits variability based on both frequency and antenna characteristics. This variability introduces nuanced outcomes in reflector height estimation when multiple frequencies are employed, necessitating an exploration of the Inter-Frequency Bias (IFB) (Larson et al., 2023).

Antenna Phase Centre Variation

The antenna phase centre, a critical consideration in GNSS-IR, exhibits frequency-dependent variations. This variation is not solely contingent on the frequency but is also influenced by the specific characteristics of the antenna. As a consequence, the incorporation of multiple frequencies in GNSS processing can yield disparate results for reflector height estimation (Larson et al., 2023).

Mitigation of the Inter-Frequency Bias

To address the challenges posed by IFB, a common practice involves mapping the signal corresponding to a particular frequency onto the GPS L1 signal (G01). This process facilitates the alignment of signals at different frequencies, allowing for more consistent and accurate reflector height estimates (Williams, 2023).

1.2. Multipath and GNSS-IR

Amidst the multiple factors affecting GNSS accuracy, such as clock inaccuracies, ionospheric and tropospheric delays, one prominent source of error significantly impacts the reliability of GNSS positioning data: multipath effects. Multipath effects arise from signal reflections, where the satellite signal encounters surfaces in close proximity to the receiver, including buildings and bodies of water. The multipath effect is driven by the instantaneous excess propagation delay d of a reflection with respect to the direct path

$$d = 2H \cdot \sin(e) \tag{1.4}$$

where H is the vertical distance of the antenna phase centre above the reflecting surface and e is the elevation angle of the satellite with respect to the horizon (Georgiadou & Kleusberg, 1988)(Larson, Löfgren, et al., 2013). Conventionally, multipath signals are considered detrimental and efforts are directed towards their suppression. Nevertheless these effects can be used to gather valuable information about the reflecting surfaces they originate from, for example in GNSS-Interferometric-Reflectometry (GNSS-IR).

Unlike other GNSS applications that rely on carrier phase and pseudo-range data, GNSS-IR leverage of these multipath effects to compute reflector heights H. As satellites traverse a receiver's field of view, the changing angle of signal

reflection alters the multipath delay. This phenomenon results in the creation of an interference pattern, encapsulated within the satellites Signal-to-Noise Ratio (SNR) data. Figure 1.1 illustrates the basic principles of GNSS-Interferometric-Reflectometry. The direct signal (blue) is reflected on the surface (red) and delayed (1.4), introducing an interference to the signal. Depicted in the centre are examples of the interference pattern created by the reflected signal being in phase with the direct signal, thus enhancing the signal strength or out of phase dampening it.

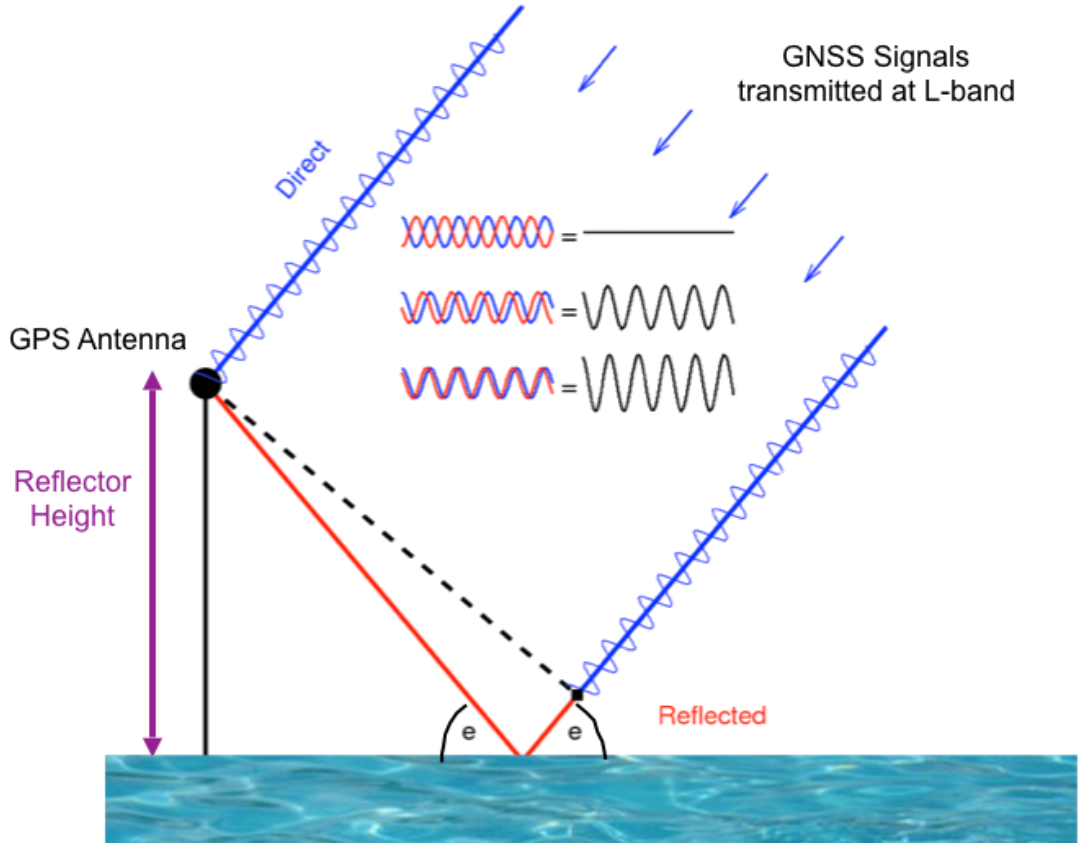

Figure 1.1.: *Basic sketch of the GNSS-IR functionality, as pictured in Larson (2023b)*

The SNR data, carrying the necessary information, derives from the carrier tracking loop outputs of the GNSS receiver, presented in the form of a phasor diagram (figure 1.2). The diagram visualises the amplitude and phase relationships between the in-phase (I) and quadrature (Q) channels of the receiver. Represented as an arrow in a complex plane, the phasor encapsulates a complex number, portraying a sinusoidal quantity. The in-phase component corresponds

to the real part of the received signal, aligned with the carrier wave, and conveys both amplitude and phase information. Simultaneously, the quadrature component serves as the imaginary part of the received signal, also carrying amplitude and phase information but shifted 90 ° from the in-phase channel, hence referred to as the quadrature component. The utilisation of quadrature channels enables the receiver to execute complex signal processing operations, including demodulation and decoding, encompassing both amplitude and phase.

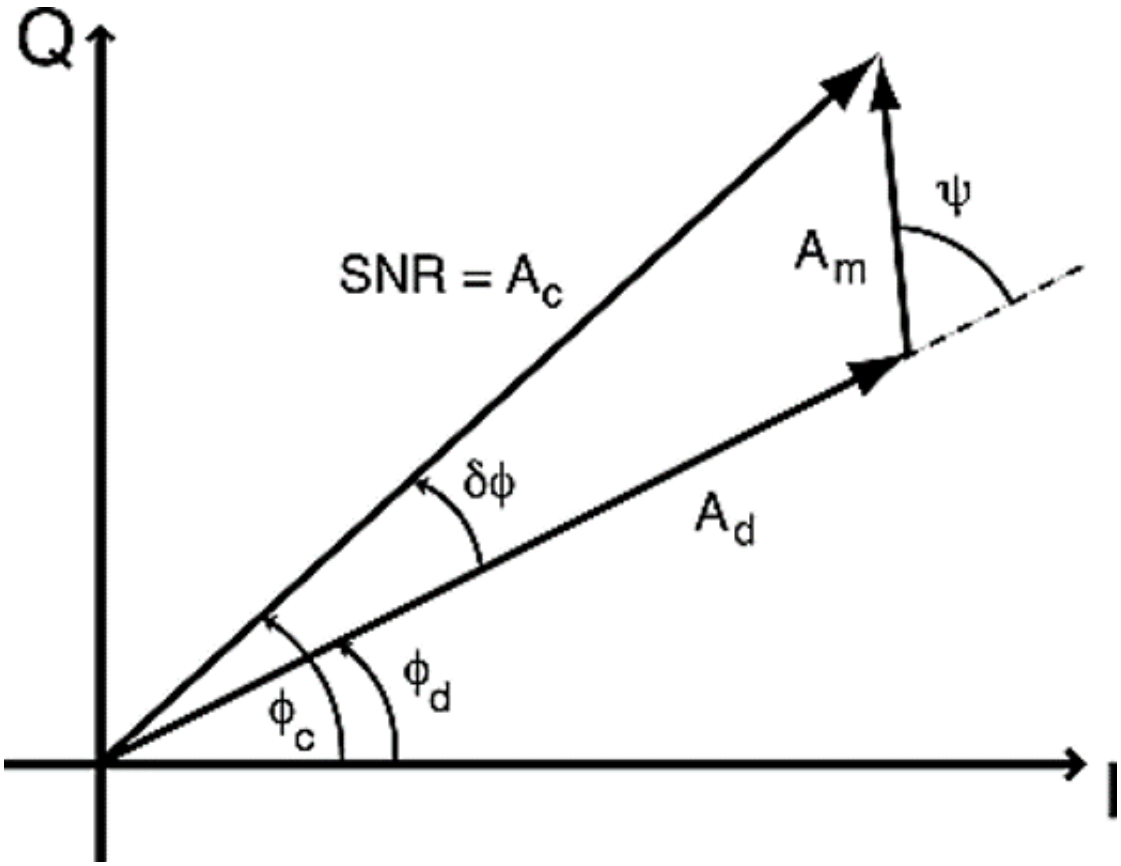

Figure 1.2.: *Phasor diagram describing the amplitude and phase relationships between I and Q channels used in the carrier tracking loop, as pictured in Bilich and Larson (2007)*

The length and angle, with respect to the I-axis, of the phasor arrows signify the amplitude and the phase angle of the signal. Here A_d, A_m and A_c denote the amplitudes of the direct, multipath and composite signal, respectively. Similarly ϕ_d and ϕ_c represent the corresponding phases of the direct and composite signals.δ_ϕ and ψ denote the multipath error and the multipath relative phase. With the introduction of multipath reflections, additional contribute to the

diagram. The SNR data then transforms into a measurement of the composite signal amplitude, resulting from the vector sum of all phasors within the diagram. Through the application of the law of cosines and the geometric relationships illustrated in Figure 1.2, the SNR data can be expressed as

$$\mathrm{SNR}^2 = A_c^2 = A_d^2 + A_m^2 + 2A_dA_m\cos\psi \tag{1.5}$$

By incorporating the wavelength λ into equation (1.4), the path delay d can be expressed as spatial equivalent to the multipath relative phase ψ. This leads to

$$\psi = \frac{2\pi}{\lambda}\cdot d = \frac{2\pi}{\lambda}\cdot 2H\cdot\sin(e) \tag{1.6}$$

The SNR data also encompasses information regarding the combined effects of satellite power transmission levels and the antenna gain pattern, carried by the direct signal. Larson (2023b) emphasises the necessity of removing these effects using a low-order polynomial (typically of order 2 to 4), leaving the SNR data with the direct signal isolated and removed. The SNR data for a single satellite can then be modelled as

$$\mathrm{SNR}(e) = A(e)\cdot\sin\left(4\pi\frac{H}{\lambda}\sin(e)+\phi\right) \tag{1.7}$$

Where e, λ, ϕ, H, and $A(e)$ respectively stand for the elevation angle, GNSS wavelength, phase offset, vertical distance between the reflecting surface and the antenna (phase centre), and the amplitude of the SNR data (Roesler & Larson, 2018). Figure 1.3 and figure 1.4 show the SNR data for satellite PRN 9 (GPS L1) with and without the direct signal contribution over the sine of elevation.

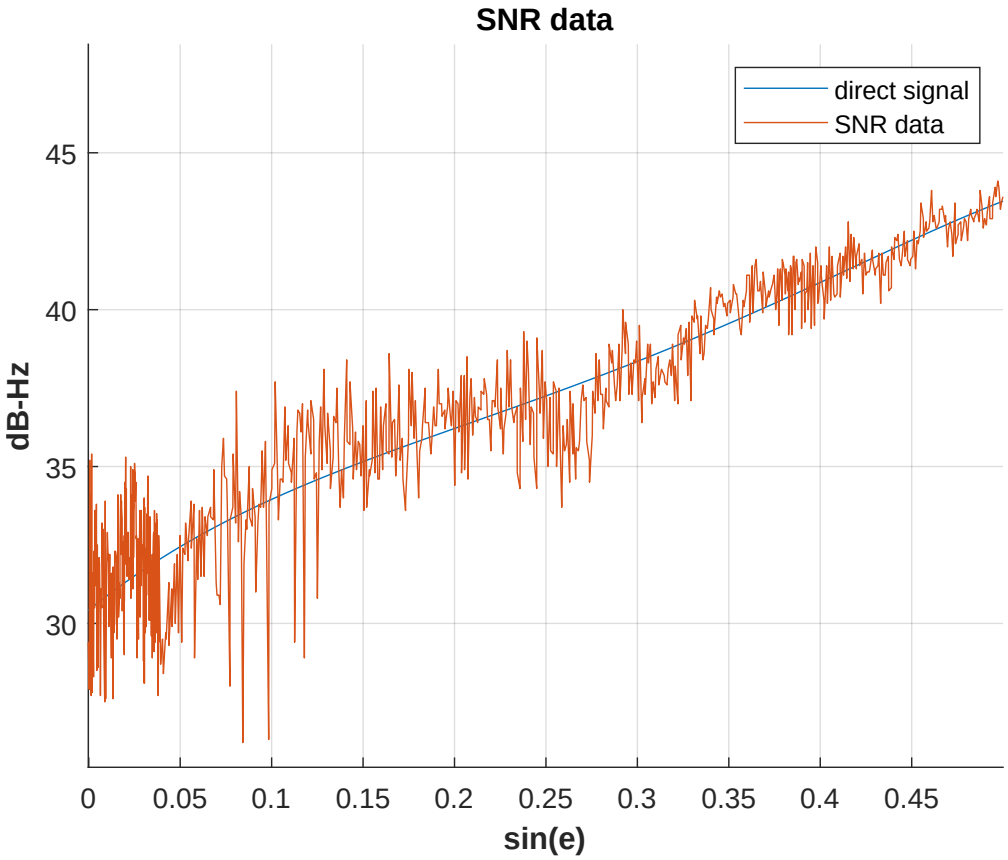

Figure 1.3.: *SNR data in dB-Hz over* $\sin(e)$ *for satellite PRN 9, GPS L1 day 127*

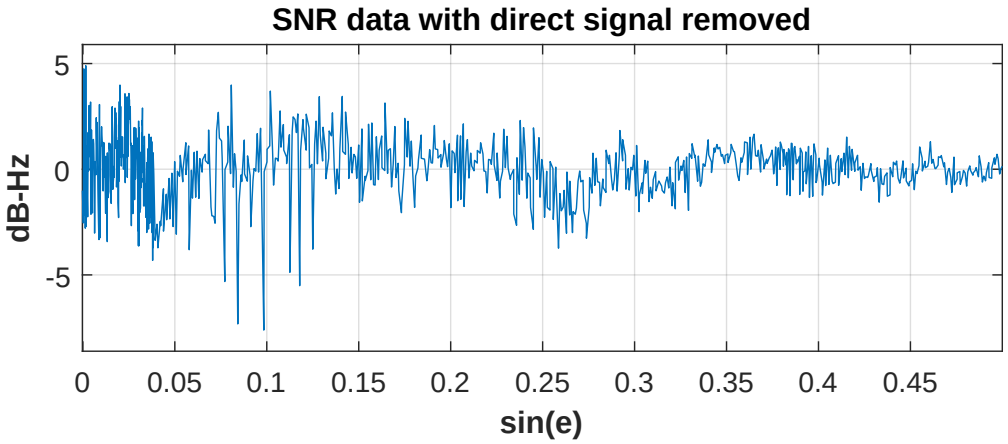

Figure 1.4.: *SNR data in dB-Hz over* $\sin(e)$ *with direct signal removed for satellite PRN 9, GPS L1 day 127*

The interference pattern yields periodic oscillations in the SNR data of each satellite track and the frequency of these interference patterns provides critical insights into the vertical distance between the antenna phase centre and the reflecting surface. As described by Karegar et al. (2022), the inherent multipath frequency f of the oscillations is primarily contingent on the wavelength (λ) of the GNSS signal

$$f = \frac{2H}{\lambda} \tag{1.8}$$

By estimating this frequency, H can be determined, and consequently, the water level can be derived.

The SNR data is naturally time-sampled, however in GNSS-IR, the essential information required for reflector height calculations is dependent on the elevation angle of each satellite. Bilich and Larson (2007) and Axelrad et al. (2005) have shown that multipath frequencies for a horizontal and planar reflector, such as a river surface, change as a satellite traverses the receiver. Furthermore Axelrad et al. (2005) introduced a variable shift from using the elevation angle to the sine of the elevation, leading to a multipath frequency for each ascending and descending arc of a satellite. This non-uniform sampling along the sine of elevation necessitates the utilisation of a Lomb-Scargle-Periodogram, a statistical tool designed to identify significant peaks in the amplitude of each satellite's signal. These peaks, once detected, correspond to the estimated reflector height for the respective satellite traverse (Larson, 2023b). Although the amplitude data is dependent on the elevation, it is still time-dependent because e (and hence $\sin(e)$) is a function of time (Nievinski & Larson, 2014).

1.3. Water Level Monitoring

Usually, water level monitoring in water bodies, such as rivers, is realised through (stream-) gauges positioned at significant locations such as bridges, water gates and sluices. These gauges employ various stage measurement methods including staff gauges, floating or pressure gauges, radar, and ultrasound (Wikipedia, 2023). Gauges are used to indicate the water level above a reference point known as gauge zero. The gauge zero can be determined through precise measurements to three fixed points in the DHHN2016 (Deutsches Haupthöhennetz 2016) and positioned beneath the riverbed but above the lowest measured water level over an extended period ensuring measurements even at minimum and maximum water levels while avoiding negative values. The final water level determination involves measuring the water height at the gauge (typically in

cm), and combining it with the established gauge zero (Wasserstraßen- und Schiffsverwaltung des Bundes, 1999). Stage measurements are categorised into contact and non-contact methods. Contact methods such as staff gauges and floating or pressure gauges are in direct contact with the water. Staff gauges visually indicate water levels and are often complemented by other gauge types for comprehensive insights into water levels and flow rates (Sauer & Turnipseed, 2010). Floating gauges utilise a float connected to a graduated steel tape, a lead or stainless-steel counterweight and a pulley wheel. A shaft encoder is connected to an electronic distance measurement device where time measurements of the stage are recorded (Sauer & Turnipseed, 2010). Pressure gauges measure pressure differences instead of water levels. Therefore a gas, such as nitrogen or air is forced through a fixed orifice mounted in the stream. Through a gas tube the water pressure is transmitted to a pressure sensor where it is converted to a stage measurement (Sauer & Turnipseed, 2010). Non-contact methods are generally positioned above the water surface. Ultrasound uses a high frequency acoustic transducer to propagate sound waves through the air to the water surface and measure the reflection. However, Sauer and Turnipseed (2010) states, its accuracy is influenced by air temperature and density. Similar to Ultrasound and GNSS-IR, radar gauges operate above the water surface. They emit radar signals, calculating water surface stage height based on the time delay between signal transmission and reception - much like GNSS-IR (Sauer & Turnipseed, 2010). By replacing the radar signal transmitter with satellite signals and employing a GNSS receiver or, in this study, a SAPOS-Station, the radar gauges develop a resemblance with GNSS-IR.

1.3.1. Importance of Water Level Knowledge

Accurate knowledge of water levels in rivers, lakes and oceans is critical for various ecological and economical reasons. In coastal areas, precise water level data aids in predicting hurricane-inundation and safeguarding coastal ecosystems (Sauer & Turnipseed, 2010). For shipping, understanding river water levels is vital for determining passage height at bridges and ensuring sufficient fairway depth for ships. The fairway represents a designated area in a river where minimum depths are guaranteed, impacting navigational safety (SWR, 2023). In operational hydrology, water level data is fundamental for studying changes in water levels, providing insights into aquatic habitats, environmental impacts, and acting as a basis for early warning systems, particularly for potential floods (Wikipedia, 2023).

1.3.2. GNSS-IR as an Alternative Method

This study explores the potential of GNSS Interferometric Reflectometry (GNSS-IR) as an alternative to traditional stream gauges for water level monitoring. Leveraging the existing GNSS infrastructure of the SAPOS Network in Germany, GNSS-IR offers a cost-effective and easily employable alternative. By capturing signals from Global Navigation Satellite Systems and analysing interference patterns, GNSS-IR enables water level determination without the need for dedicated gauge installations. This accessibility and efficiency make it a promising method in various environmental settings.

1.4. SAPOS

The German satellite positioning network, SAPOS, is a joint project operated by the Working Committee of the Surveying and Mapping Agencies of the Laender of the Federal Republic of Germany (AdV). Comprising over 270 GNSS reference stations within Germany and an additional 30 stations in neighbouring countries, SAPOS has played a pivotal role since its establishment in 2001, offering a permanent, multi-functional, and differential GNSS service. SAPOS's primary function is to compute highly precise correction data for 3D spatial reference in the European Terrestrial Reference System 1989 (ETRS89). This capability facilitates exceptionally accurate position determination in terms of both location and height, incorporating data from multiple GNSS constellations. As highlighted by Riecken and Kurtenbach (2017), SAPOS provides data with horizontal accuracy exceeding 1 cm and vertical accuracy of up to 1 cm. The use of SAPOS data has significantly improved the accuracy of the DHHN2016. With the introduction of spatial reference 2016, SAPOS incorporated the German Combined Quasi-Geoid (GCCG2016) as an optional but integrative feature for its services. The GCG2016 enables the immediate determination of normal heights with accuracy of 10 mm up to 1000 m terrain height and 25 mm above 1000 m terrain height (Riecken & Kurtenbach, 2017). While SAPOS services currently rely on differential GNSS positioning, future developments are anticipated to incorporate Precise Point Positioning (PPP) methods. This advanced approach involves precise modelling and error elimination by the rover itself, eliminating the need to communicate with a base station. This is particularly advantageous for mobile applications, such as autonomous driving. The introduction of the new PPP-RTK service is slated to come online by January 1, 2025, marking a significant step towards further advancements in precise positioning within the SAPOS network (Zentrale Stelle SAPOS, 2023).

1.5. RINEX Format

The Receiver Independent Exchange Format (RINEX) was developed for the uncomplicated exchange of GPS data during EUREF 89, the first large European GPS campaign, by the Astronomical Institute of the University of Bern. It was based on the fact that most geodetic processing software relies on specific sets of data, the carrier-phase measurement and the pseudorange measurement as well as the observation time. Station name, antenna height and other station related information were needed too. Until today RINEX provides a reliable global exchange format for GNSS data which is used by most GNSS applications (International GNSS Service (IGS),RINEX Working Group and Radio Technical Commission for Maritime Services Special Committee 104 (RTCM-SC104), 2018).

1.6. Related Methods

GNSS-IR is only one of several techniques to remotely sense the Earth's surface. Other established methods include Radar Altimetry, Radar Interferometry and GNSS-Reflectometry (GNSS-R). Although they all share basic principles, every method holds unique strengths and applications to its name, which are discussed in this section.

1.6.1. Radar Altimetry

Radar Altimetry operates by transmitting high-frequency signals from satellites to Earth and analysing the echoes received from the surface, by precisely measuring the time taken for the round trip of a radar pulse between the satellite and the surface. These time measurements, scaled to the speed of light, yield the range measurements. With knowledge of the satellites altitude and the range measurements one can determine the difference in height between the sea surface and the satellites reference ellipsoid (sea surface height). Critical orbital parameters are altitude inclination and orbit period. The satellites altitude is derived from precise knowledge of the satellites orbit, including factors like inclination, atmospheric drag, gravity forces acting on the satellite and the area of the world to be mapped, thus determining precise orbits is crucial for radar altimetry. The main techniques to accomplish that are to compute the satellites trajectory relative to Earth, by using the Doppler shift to accurately

determine the velocity of the satellite on its orbit, and dynamic orbitography models to deduce the satellite trajectory relative to Earth (e.g. DORIS or PRARE instruments), usage of GNSS systems or laser tracking. Furthermore, to achieve accurate measurements, radar altimeters must correct for electromagnetic wave deceleration. These corrections are essential for ensuring the precision of range measurements (Rosmorduc et al., 2011).

1.6.2. Radar Interferometry

Radar Interferometry utilises the coherence of Radar systems to extract valuable scatter- and phase-information, enabling applications such as the generation of digital height models, detection of surface changes in the centimetre range and classification of moving scatterers. Two modes, the single-pass mode and the repeat-pass mode, are employed in Radar Interferometry. In the single-pass mode, two separate antennas scan a target area during the same pass, while the repeat-pass mode traverses the target location multiple times, scanning a specific area at least twice. Depending on the direction of the spatial distance between the antennas (baseline), these methods are categorised as along-track or across-track interferometry. The measured phase-information is sensitive to changes in the distance between the radar and the target, as well as changes in the surface properties of the target (Madsen & Zebker, 1998). The interferometric phase is a measure of the difference in phase between two radar signals that are combined. If the baseline is sufficiently small, the scattering behaviour can be assumed to equalise itself, leaving the interferometric phase as the difference in distance between the antenna positions and the scatterer. The critical baseline depends on wavelength, distance between the sensor and scatterer, and the angle of incidence, affecting resolution and sensitivity. Measurements of phase differences however are limited to modulo 2π, leading to an ambiguity. Phase-unwrapping, commonly based on the integration above the phase gradient derived from the interferometric phase, is applied to resolve this ambiguity (Madsen & Zebker, 1998). The height above an arbitrary surface (reference ellipsoid) can then be computed with basic trigonometric equations using the interferometric phase. Several factors can impact the effectiveness of radar interferometry including Signal-to-Noise Ratio (SNR), geometric decorrelation (growing with baseline), and time decorrelation (repeat-pass applications). However, time decorrelation can be utilised with the absolute normalised complex correlation coefficient to determine changes in the scattering area, facilitating the derivation of a classification model. Multiple height models can be used to compute differential height models which contain information

about relative changes in topography in the area of a few centimetres, therefore they are often applied in volcanic studies and monitoring of glaciers. Other applications include tomography, where multiple baselines are used to compute 3-dimensional data sets and polarimetric interferometry, where the polarisation is varied to receive different resolutions, enabling the computation of height models for the leaf canopy and the ground of the corresponding scattering cell to derive vegetation height models (Martin et al., 2017).

1.6.3. GNSS-Reflectometry

Since the late 1980's the idea of using GNSS signals for remote sensing of the Earth's Atmosphere and Earth's surface scatterometry, the determination of the surface roughness, were discussed by Hall and Cordey (1988) and later even for ocean altimetry by Martin-Neira et al. (1993). In 1998 Katzberg and Garrison demonstrated that GNSS signal reflections can sense ocean surface roughness and related wind (Garrison et al., 1998; Lin et al., 1999). In 2000, Komjathy et al. (2000) provided an idea to explore the method to realise cryospheric remote sensing of the Earth's frozen regions, especially for sea and freshwater ice and frozen ground. The basic idea involved using the reflection of the GNSS signals to determine information on the reflecting surfaces such as its location, roughness and dielectric properties. The technique to realise thus involves measuring the correlation power of the signals at different delays and Doppler values (Komjathy et al., 2000). This technique to remotely sense various types of surface properties with a bi-static or, considering that a GNSS receiver can receive multiple satellite signals, multi-static radar of opportunity is called GNSS-Reflectometry (GNSS-R) (Zavorotny et al., 2014). GNSS-R utilises the pseudoranges and the Doppler measurements by the receiver and the time delay and frequency change by the reflected signal to obtain the Delay Doppler Map (DDM). As described in Zavorotny et al. (2014) the DDM is a representation of the reflected and scattered signal as a function of the delay and Doppler frequency. The delay portrays the time delay between the transmitted and received signals, while the Doppler frequency represents the frequency shift due to the relative motion between the transmitter and the scatterer. The scattered signal originates from the glistening zone, which represents the surface of the Earth, where the reflected waves arrive from. It is the area where the diffuse, quasi-specular scattering process occurs and its centred on the nominal specular direction, coming from an area much larger then the FFZ (First Fresnel Zone). To obtain the DDM the recorded signal is cross-correlated with the PRN (pseudo random noise). It is a key product of GNSS bi-static radar, as

it contains information about the surface roughness, wind speed, and other geophysical parameters. The DDM therefore enables various applications for weather forecast and climate research, i.e. tsunami detection and hurricane forecasting.

1.6.4. Inverse Method

The Inverse Method offers an alternative to the spectral analysis used in other GNSS-R techniques, by adopting a focus on physical models for data analysis. In this approach, an analytic function is meticulously fitted to the Signal-to-Noise Ratio (SNR) oscillations. The representation of water level variations employs B-splines, which are approximations of splines using weight functions (Strandberg et al., 2016). B-splines, characterised by $n + 1$ control points determined by the user, define a C^2-Curve, where the direction and curvature are consistently changing (Wittmers & Gensel, 2006). The determination of B-spline coefficients is accomplished through a nonlinear least squares fit. The selection of consistent model parameters facilitates the integration of data from multiple GNSS systems into a single inversion process. As highlighted by Strandberg et al. (2016), this method yields increased accuracy compared to other GNSS-R techniques.

2. Methodology

GNSS-Interferometric-Reflectometry (GNSS-IR), an innovative remote sensing method of monitoring surface changes on Earth, such as water level, has emerged through the fast-growing GNSS networks and the pioneering research by Prof. Kristine M. Larson. Their landmark studies, especially the accidental tide gauge by Larson, Ray, et al. (2013), Löfgren and Haas (2014), have demonstrated the remarkable capability of GNSS-IR in measuring coastal water levels. GNSS-IR has been utilised in various applications nowadays, especially looking at measuring snow depth, soil, and soil moisture (Larson & Nievinski, 2013) (Larson et al., 2008). As Roesler and Larson (2018) described (1.7) can be used for diverse purposes. If H is fixed, changes in ϕ are used to derive soil moisture . Variations in $A(e)$ can be leveraged to measure vegetation water content (Wan et al., 2015) as well as to detect sea ice (Strandberg et al., 2017). To facilitate broader exploration of GNSS-IR's potential, Prof. Larson has developed a user-friendly software and a corresponding website, providing accessibility to GNSS-researchers and enthusiasts alike. This software not only serves as a valuable tool for individual exploration but is also instrumental in validating the applicability of GNSS-IR at SAPOS stations for this study.

This study focuses on implementing GNSS-IR for water level monitoring at the SAPOS station in Iffezheim, located near Karlsruhe in southwest Germany. The methodology involves the computation of reflector heights from RINEX 3.04 files, generously provided by the Landesamt für Geoinformation und Landentwicklung (LGL), that cover a time period of 300 days in 2023. The files start with the 01. January 2023 and span a period up to the 27. October 2023.

In this chapter, the step-by-step procedure for utilising the GNSS-IR software by Prof. Larson, hereafter referred to as *gnssrefl*, on the specific data set from Iffezheim is elucidated. The process involves several key-steps to derive daily average water levels, and if desired even sub-daily water levels:

1. **Site evaluation**

   Evaluate the site comprehensively, considering the source of reflections (water surface), antenna height, and other pertinent factors.

2. **Fresnel Zones and Nyquist Calculation**

   Compute Fresnel zones and determine the Nyquist frequency to assess the capabilities of the site accurately.

3. **Data Preparation**

   Convert RINEX 3.04 files into Signal-to-Noise Ratio (SNR) data, a crucial step in preparing the data set for further analysis.

4. **Development of an Evaluation-Strategy**

   Utilise Lomb-Scargle-Periodogram to perform a comprehensive frequency analysis, deploying a strategy that incorporates quality control measures

5. **Reflector Height Computation**

   Execute the code to calculate reflector heights utilising the established strategy.

6. **Daily Average Computation**

   Implement the *daily_avg* module to compute a daily corrected average water height for each day of data. This involves applying a median filter and removing the inter-frequency bias, ensuring the reliability of the derived water levels.

2.1. Site Evaluation

The initial phase of data evaluation involves a careful examination of the site specifics in Iffezheim and the preparation of essential Signal-to-Noise Ratio (SNR) data for the *gnssrefl*-program. The GNSS antenna is strategically positioned on top of a building at the Iffezheim Rhine-sluice, standing at an approximate height of 14 m above the water surface. This facility is under the jurisdiction of the Wasserstraßen- und Schifffahrtsamt Oberrhein, and the provided GNSS data is managed by the Landesamt für Geoinformation und Landentwicklung (LGL) in Baden-Württemberg. The site's characteristics present distinct challenges for GNSS-IR application. Notably, the Northern quadrants are already part of the sluice-structure and hold no useful water surface for reflections at all. Conversely, the southern quadrants offer favourable visibility, although complicated by an elongated pier directly below the building, spanning an approximate azimuth range of 185 to 200 degrees. The antenna's elevation, ranging between 12 to 14 m above the surface, provides an extensive view over a significant portion of the southern quadrants, facilitating reflections. Screenshots taken from Google Earth and the Wasserstraßen- und Schiffsverwaltung des Bundes (n.d.)-Website are depicted in figures 2.2 and 2.1 below.

Figure 2.1.: *Google-Earth screenshot of the site in Iffezheim*

(a) *Sluice Iffezheim looking north* ***(b)*** *Sluice Iffezheim looking south*

Figure 2.2.: *WSV screenshots of the sluice in Iffezheim*

2.2. Fresnel Zones and Nyquist Frequency

2.2.1. First Fresnel Zones

To delve deeper into the site's usability, the computation of Fresnel zones becomes imperative. In the realm of GNSS Interferometric Reflectometry (GNSS-IR), these zones play a pivotal role in predicting regions where satellite signals reflect off a surface and produce interference in the signal. The calculation of these reflective zones is critical for understanding the site's capabilities and anticipating regions where valuable data may be obtained. Particularly, the First Fresnel Zone (FFZ) assumes significance in this analysis. The FFZ is a conceptual rotation ellipsoid positioned between the GNSS antenna and the reflecting surface, its size is directly sensitive to the vertical distance to the antenna, the elevation angle, and the transmitter frequency. The computation of FFZ relies on the well-established formula for ground-based installations by Hristov (2000).

Starting with $n = 1$ to denote the first Fresnel zone, the formula is expressed as follows:

$$d = n \cdot \frac{\lambda}{2} \tag{2.1}$$

$$R = \frac{h}{\tan(e)} + \frac{\left(\frac{d}{\sin(e)}\right)}{\tan(e)} \tag{2.2}$$

$$b = \sqrt{2 \cdot \frac{d \cdot h}{\sin(e)} + \left(\frac{d}{\sin(e)}\right)^2} \tag{2.3}$$

$$a = \frac{b}{\sin(e)} \tag{2.4}$$

Here d, R, b and a are the parameters defining the dimension of the corresponding FFZ. The perimeter of the zone can then be expressed over the inner angle θ of [0,2π]:

$$x' = a \cdot \cos(\theta) + R \tag{2.5}$$

$$y' = b \cdot \sin(\theta) \tag{2.6}$$

Subsequently, the axes are aligned with the satellite azimuth:

$$x = \sin(\alpha) \cdot x' - \cos(\alpha) \cdot y' \tag{2.7}$$

$$y = \sin(\alpha) \cdot y' + \cos(\alpha) \cdot x' \tag{2.8}$$

Here, λ represents the wavelength, h denotes the antenna height, e and α indicate satellite elevation- and azimuth-angle. The conceptualisation and computation of Fresnel zones, especially the First Fresnel zone, serve as a fundamental framework for comprehending signal reflections in GNSS-IR. The orientation of the FFZ is contingent on the azimuth angle of the satellite, and as the elevation angle increases, the Fresnel zone becomes smaller and closer to the antenna, influencing the reflectivity of the site.

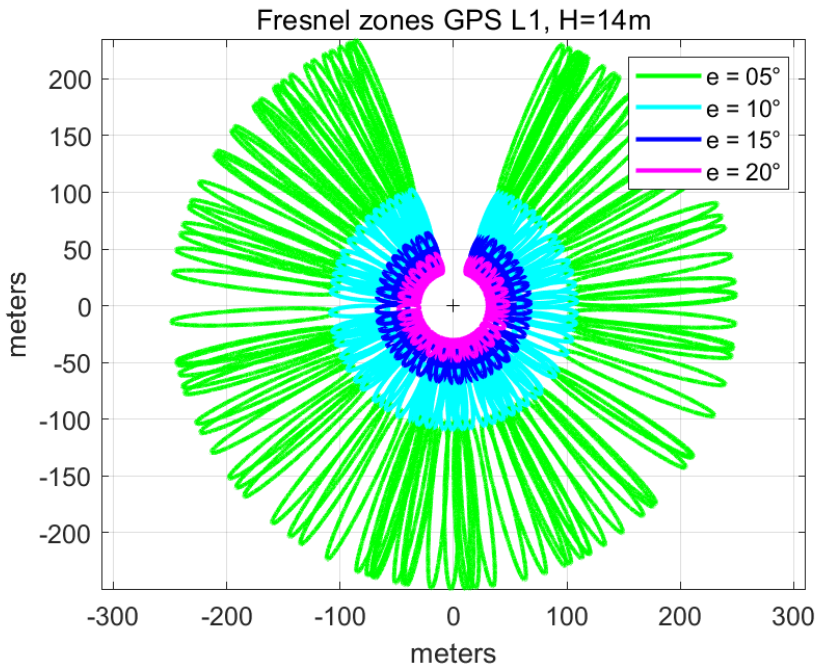

Figure 2.3.: *View of all Fresnel zones, GPS L1 day 127*

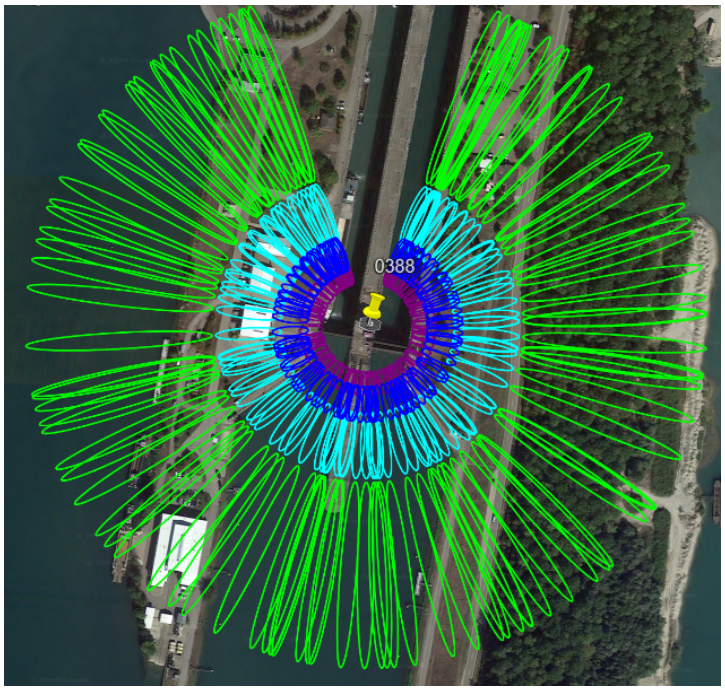

Figure 2.4.: *View of all Fresnel zones on Google-Earth, GPS L1 day 127*

Figure 2.3 displays every computed first Fresnel zone, for an estimated receiver height of 14 m. The legend shows the elevation angles in 5 °, 10 °, 15 ° and 20 °. Figure 2.4 displays the zones overlapped on a Google Earth image of the site in Iffezheim, zoomed in on the SAPOS antenna on the right lower corner.

Due to the characteristics of the site, especially looking at the elongated pier, there is a need to overlay an azimuth angle and elevation angle mask on the data. Being limited to 4 distinguished azimuth and elevation masks by the *gnssrefl*-software input, careful consideration is necessary to leverage the largest possible reflecting surface, while avoiding any surface besides the river.

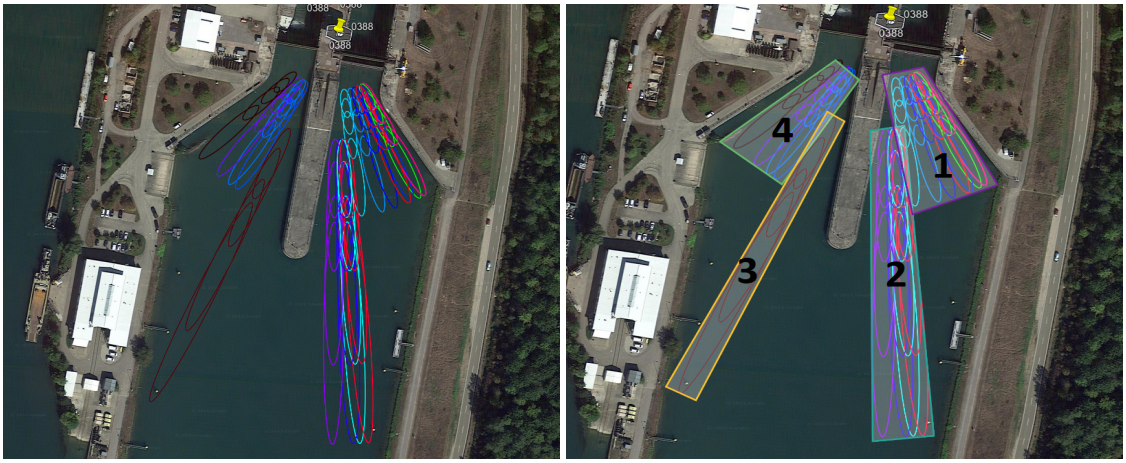

(a) *Reflections zones for Iffezheim* ***(b)*** *Individual masks for the first Fresnel zones*

Figure 2.5.: *Fresnel zones with masks applied, GPS L1 day 127*

Figure 2.5a shows the usable reflections zones for the site in Iffezheim, while figure 2.5b highlights the individual masks (1, 2, 3, 4) applied to the data. Each satellite track is represented in an individual colour.

The masks were chosen as following (deriving from the evaluation of the FFZ):

Table 2.1.: *Mask parameters for the reflection zones on the river surface*

Mask	$e_{min}[^\circ]$	$e_{max}[^\circ]$	$\alpha_{min}[^\circ]$	$\alpha_{min}[^\circ]$
1	10	20	150	175
2	5	12	175	185
3	5	10	200	210
4	10	20	210	230

2.2.2. Nyquist-Frequency

The required sampling rate is dependent on the Nyquist frequency for this site, expressed in terms of antenna height H in m. To express the SNR spectral frequencies in m, the sine of the elevation (e as a function of time t) $\sin(e(t))$ (1.2) is scaled by a wavelength factor, leading to a sampling of

$$X(t) = 2 \cdot \sin(e(t))/\lambda \tag{2.9}$$

This sampling variable X expresses the spectral frequencies directly in m, so that the Nyquist frequency for GNSS-IR purposes can be represented in terms of antenna height. According to Larson (2023a) this gives the SNR (1.7) as

$$SNR = A \cdot \cos(2\pi H X(t)) \tag{2.10}$$

Considering even sampling, anything above the Nyquist frequency will suffer from aliasing. However, the Nyquist-like limit for unevenly sampled data, much like the Nyquist frequency, marks the point where no further information from the spectral content of the sampled signal can be extracted. This limit can be larger than the common Nyquist frequency. According to VanderPlas (2018), this derives from the extra information gathered when the spacing between two samples varies, thus removing the aliasing ambiguity.

As described by Roesler and Larson, 2018, the Nyquist frequency f_c for evenly spaced data is obtained from the following formula, first computing the wavelength factor of the signal c_f, the sampling X (in inverse m), the number of data points N and the observation window W.

$$c_f = \frac{\lambda}{2} \tag{2.11}$$

$$X = \frac{\sin(e)}{c_f} \tag{2.12}$$

$$N = \text{length}(X) \tag{2.13}$$

$$W = \max(X) - \min(X) \tag{2.14}$$

This gives the Nyquist frequency (evenly spaced)

$$f_c = \frac{N}{2W} \tag{2.15}$$

And the oversampling and high-frequency factors for the Lomb-Scargle-Periodogram

$$\text{ofac} = \frac{1}{W} \cdot \frac{1}{0.01} \tag{2.16}$$

$$\text{hifac} = \frac{H_{\max}}{f_c} \tag{2.17}$$

Where 0.01 m is the desired precision for the grid spacing and $H_{\max}$ represents the maximum reflector height considered. (The sampling in inverse m is, so that the spectral content then is expressed in m.)

In summary, the interrelation between receiver sampling rate and antenna height is elucidated by the expressions (2.12), (2.13), (2.14) and (2.15). The sampling rate, influencing the quantity of data, impacts parameters such as the sampling X, the number of data points N, and the observation window W. This gives the Nyquist frequency f_c in terms of antenna height in m. As illustrated in figures 2.6, 2.7, and 2.8, a larger antenna height necessitates a higher sampling rate, and conversely, a higher sampling rate enables a larger antenna height.

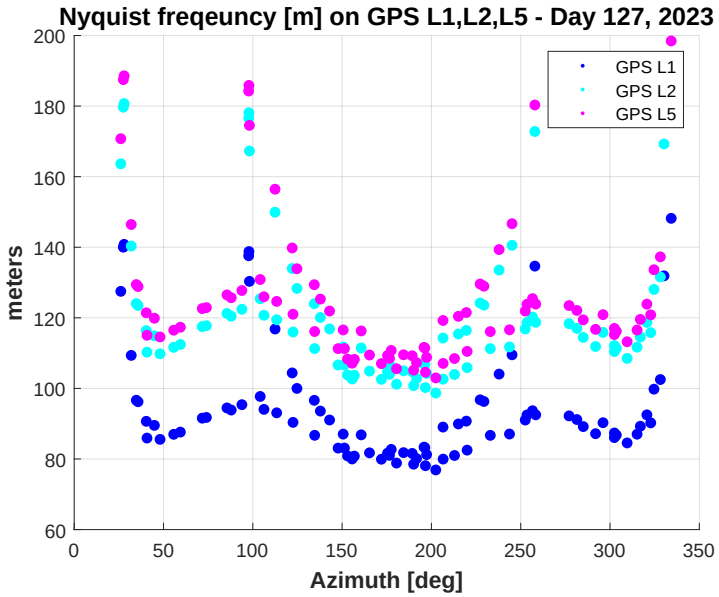

Figure 2.6.: *Nyquist frequency in terms of antenna height [m] for 5 s sampling (day 127), elevation* $5° - 20°$

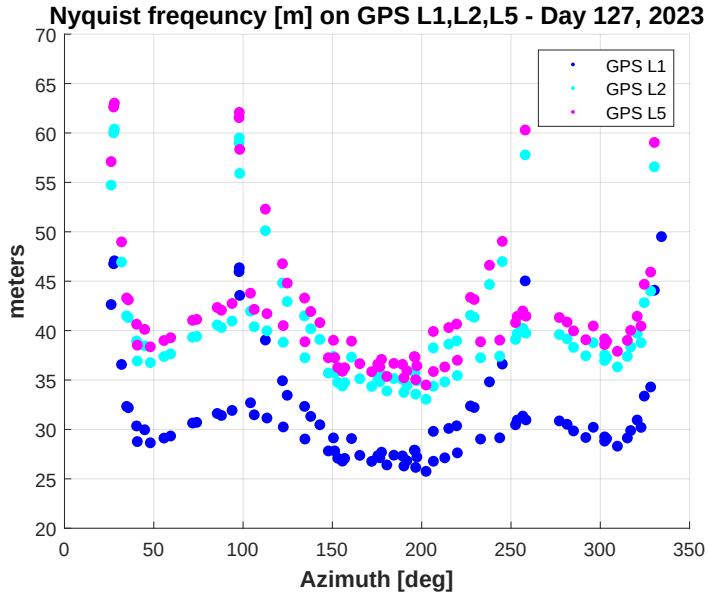

Figure 2.7.: *Nyquist frequency in terms of antenna height [m] for* 15 *s sampling (day 127), elevation* $5° - 20°$

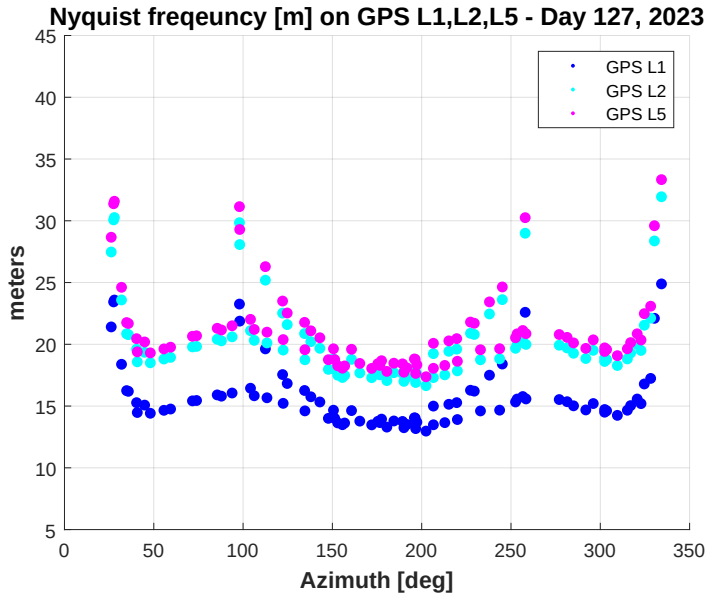

Figure 2.8.: *Nyquist frequency in terms of antenna height [m] for* 30 *s sampling (day 127), elevation* $5° - 20°$

Table 2.2.: *Median Nyquist frequencies for 5 s, 15 s and 30 s sampling rate*

Sampling Rate [s]	GPS L1 [m]	GPS L2 [m]	GPS L5 [m]
5	90.2	104.3	111.6
15	30.2	34.9	37.4
30	15.2	17.5	18.8

Nyquist plots for receiver sampling rates of 5 s (Figure 2.6), 15 s (Figure 2.7), and 30 s (Figure 2.8) are displayed above. The median Nyquist frequency values for each sampling rate are summarised in Table 2.2. Considering the height of the antenna, at approximately 14 m, it is evident that a 30 s receiver sampling rate is impractical for GNSS-IR at the Iffezheim site, particularly concerning the GPS L1 frequency. A sampling rate of at least 15 s is deemed necessary, with a 5 s rate being preferable due to the additional data it provides. In summary, the analysis indicates that the given 15 s sampling rate of the RINEX data provided by the LGL is sufficient for the GNSS-IR purpose at the Iffezheim site.

2.3. Data Preparation

Before implementing the GNSS-IR strategy, the SNR data from the RINEX 3.04 files is extracted using the *rinex2snr* module within the *gnssrefl* software. This module generates an SNR file for each RINEX file, corresponding to each day of the data. The extraction involves obtaining satellite numbers and their corresponding SNR data from the RINEX file. This information is then combined with satellite elevation angles and azimuth values from orbit files, obtained from the GFZ - GeoForschungsZentrum Potsdam, along with seconds of the day in GPS time. The command used for creating the SNR files is as follows:

rinex2snr 03880oDEU 2023 1 -doy_end 300 -snr 66 -orb gnss -samplerate 15 -stream R -nolook T -overwrite T

Here, *rinex2snr* is the command name, *03880oDEU* is the station name, *2023*, *1*, and *doy_end 300* respectively stand for the year, the day-of-year of the first RINEX file, and the day-of-year of the last RINEX file, *snr 66* instructs *gnssrefl* to save all data with elevation angles less than 30 deg, *orb gnss* indicates the use of GFZ multi-GNSS final orbits, *samplerate 15* specifies the sample rate at which the data was captured, and *stream R* indicates that the data is collected from receiver data (*S* would indicate a data stream instead). The options *nolook T* and

overwrite T are set to true, instructing *gnssrefl* to search for the RINEX files in the local directory and overwrite existing SNR files.

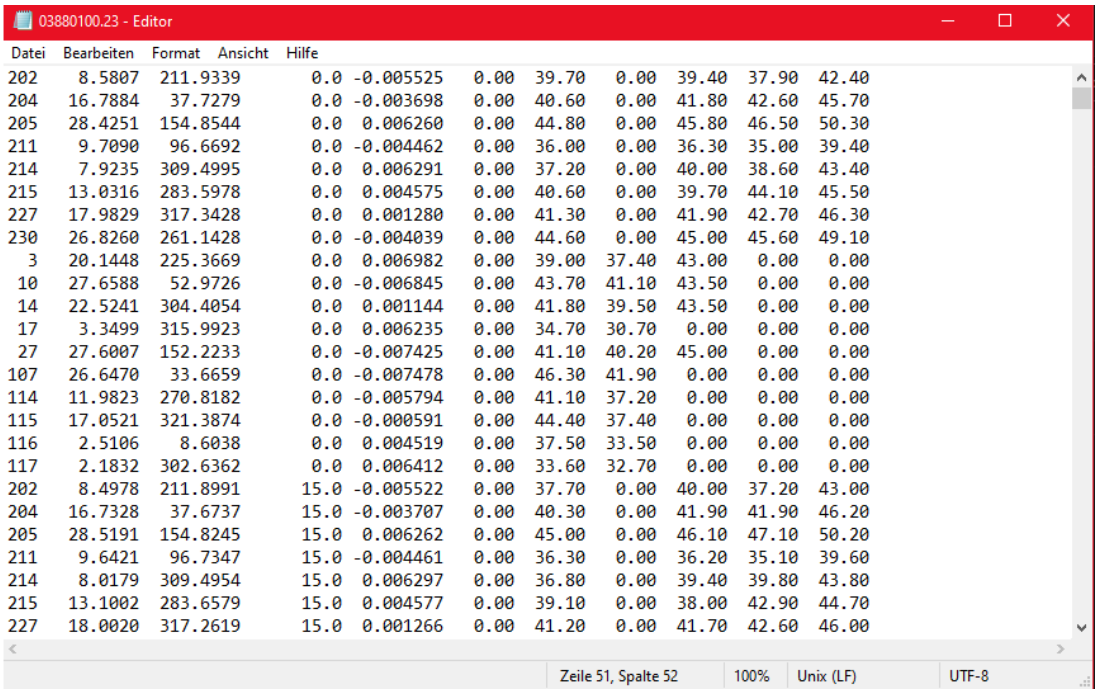

Figure 2.9.: *Example file for SNR66 data, day 10, 2023*

The columns in the SNR files are defined as:

1. Satellite number
2. Elevation angle [°]
3. Azimuth [°]
4. Seconds of the day, GPS time
5. $\dot{e}$, Elevation angle rate of change [$°/s$]
6. S6 SNR on L6 [dB-Hz]
7. S1 SNR on L1 [dB-Hz]
8. S2 SNR on L2 [dB-Hz]
9. S5 SNR on L5 [dB-Hz]
10. S7 SNR on L7 [dB-Hz]
11. S8 SNR on L8 [dB-Hz]

To distinguish between systems, 100 is added for GLONASS, and 200 for Galileo satellite numbers (the data set for Iffezheim provided no BeiDou data).

2.4. Development of an Evaluation-Strategy

2.4.1. Frequency Analysis

Once the SNR data is prepared and saved in compressed gz-format to conserve storage space, a preliminary analysis is conducted using the *QuickLook* module. This module generates Lomb-Scargle-Periodograms (LSP) for a single day of SNR data and presents them in two types of plots.

The LSP serves to identify the dominant frequency in the SNR data, directly associated with the vertical distance between the antenna phase centre and the reflecting surface. The oversampling factor and high-frequency factor play pivotal roles in this analysis. The oversampling factor ensures a fine enough frequency grid for accurate Lomb-Scargle-Periodogram computation, preventing undersampling issues and capturing peaks in the power spectrum (VanderPlas, 2018). The high-frequency factor limits the number of frequencies to optimise computation time.

Through *QuickLook* retrievals, a strategy is developed to analyse the entire data set. The command and settings for this module are chosen as follows:

QuickLook o388 2023 doy -snr 66 -e1 5 -e2 20 -h1 11 -h2 17 -azim1 150 -azim2 230 -ampl 8 -peak2noise 2.8

Here, *QuickLook* is the command name, *o388* indicates the station name, and *2023* and *doy* represent the year and day-of-year being evaluated. The option *snr 66* instructs *gnssrefl* to consider only SNR.66 data. Parameters such as elevation limits *e1*, *e2*, height limits *h1*, *h2*, azimuth limits *azim1*, *azim2* and spectral limits *ampl*, *peak2noise* are quality control measures based on the analysis of the site and Fresnel zones to effectively frame the reflecting surface without losing essential data, as done in table 2.1. The elevation-, azimuth- and height-limits derive from earlier discussions of the site evaluation (2.1), while the spectral quality control is initially determined by the following *QuickLook* plot evaluation. The values are user defined and site specific, Larson (2023b) suggests a peak-to-noise value of 2.7 for water surfaces to begin with, as well as a spectral peak amplitude value of 8.

A random set of 10 days is evaluated over every frequency in the data. The first plot provides an overview of each satellite retrieval, plotting reflector height against power levels in a linear scale for better visualisation. The second plot shows the predicted reflector height, spectral peak-to-noise value, and spectral

peak amplitude over the azimuth. For a retrieval to be accepted, both the peak-to-noise and the peak amplitude values have to be surpassed, both values are indicated by the grey dashed line in the quality control parameter plots. The reflector height summarises all accepted retrievals from the spectral quality control. Due to limited space and visualisation reasons, only the data for day 127 is shown. Observations in the northern quadrants of the Lomb-Scargle-plots are empty due to the exclusion of data below 150 ° and above 230 ° degrees azimuth. Grey retrievals indicate rejected satellite data, while coloured retrievals represent accepted data.

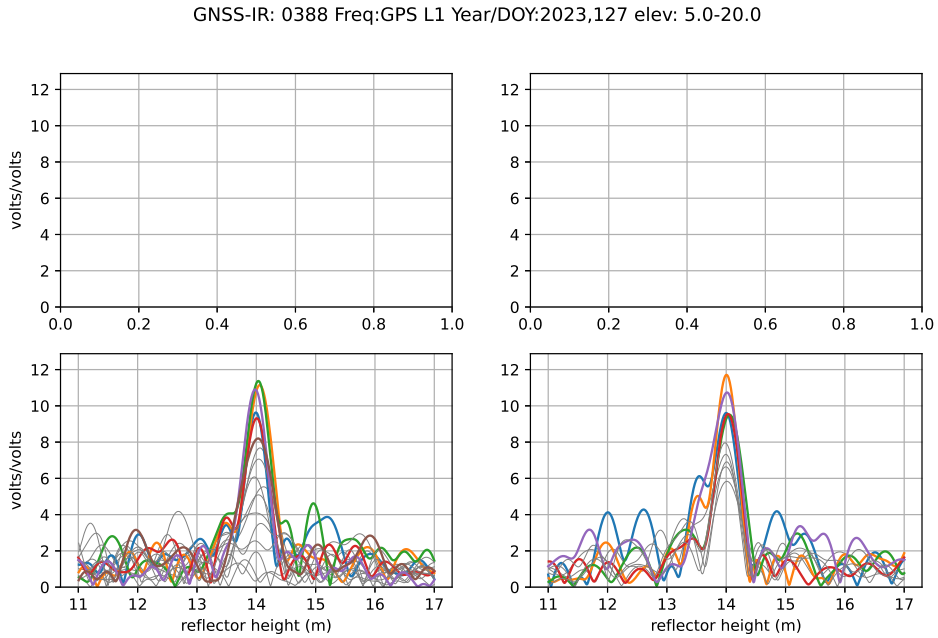

Figure 2.10.: *Lomb-Scargle plot, GPS L1,day 127*

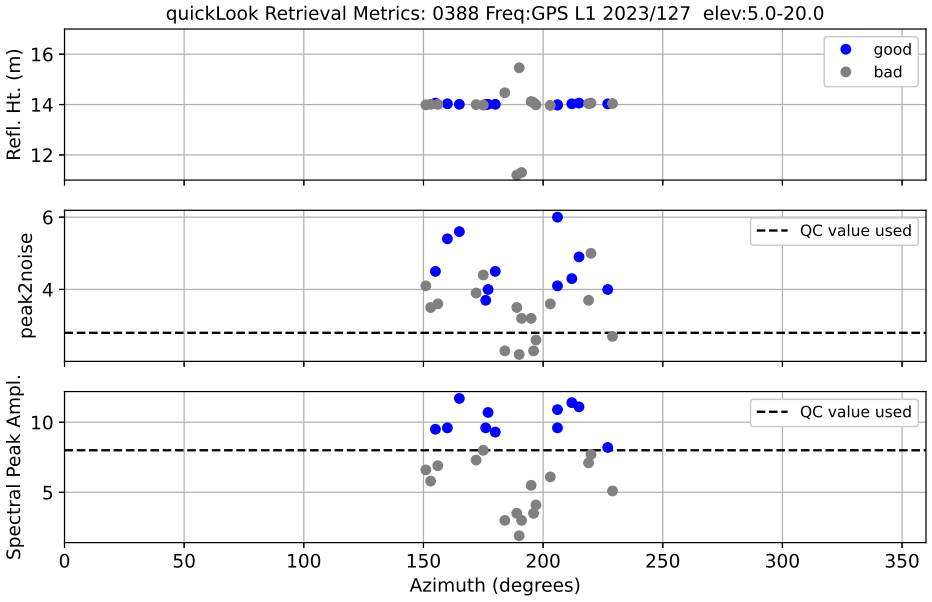

Figure 2.11.: *Spectral quality control parameters, GPS L1, day 127*

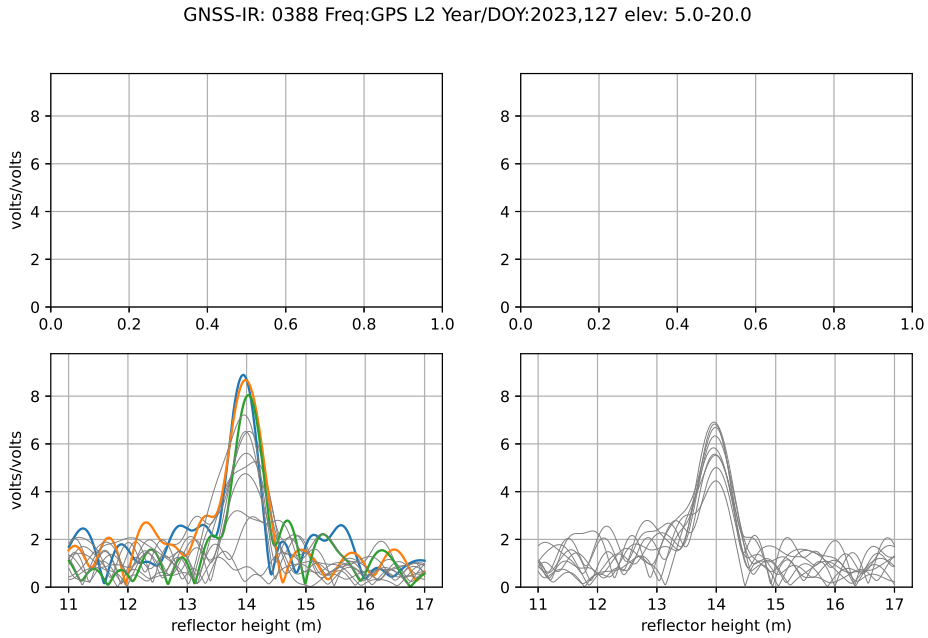

Figure 2.12.: *Lomb-Scargle plot, GPS L2, day 127*

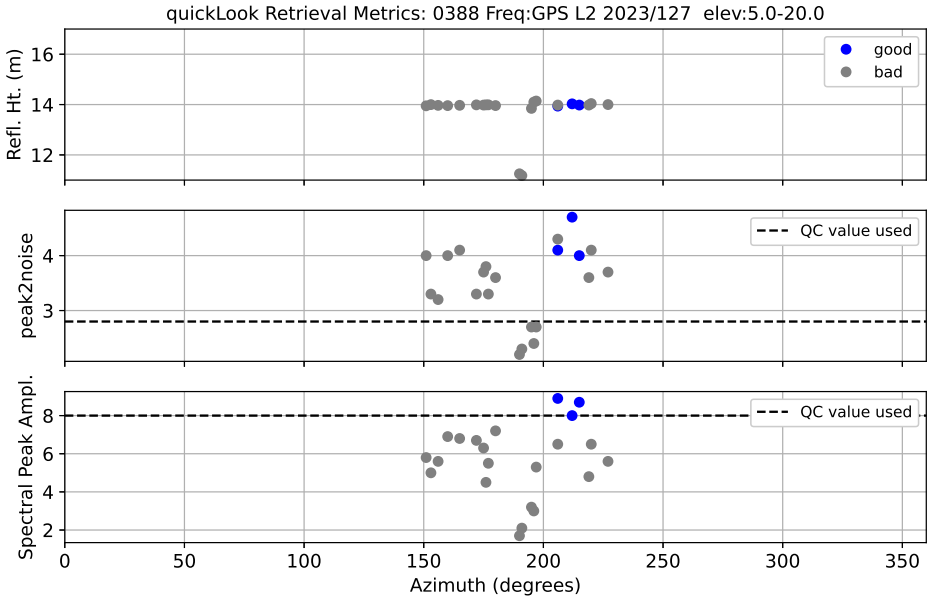

Figure 2.13.: *Spectral quality control parameters, GPS L2, day 127*

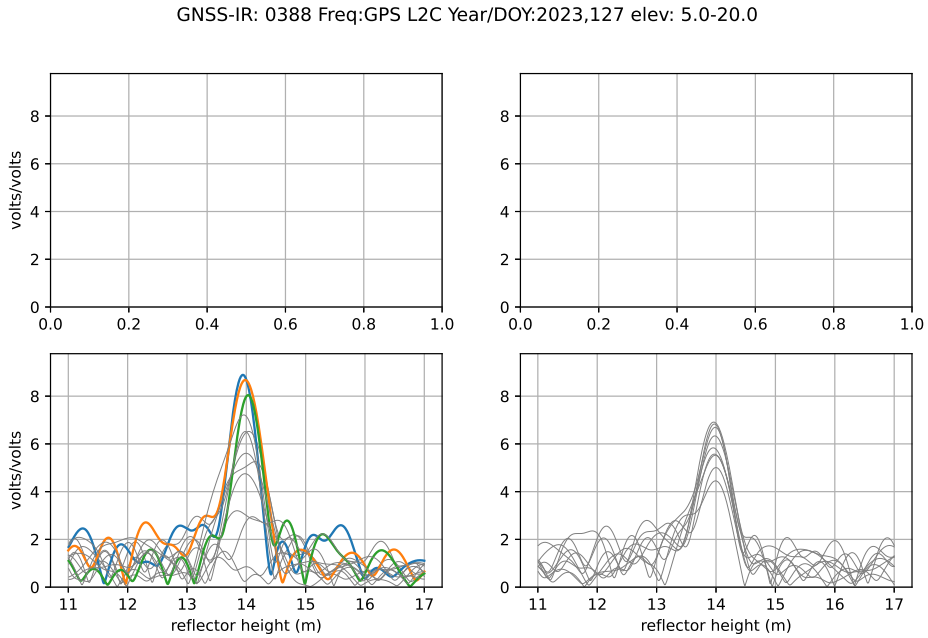

Figure 2.14.: *Lomb-Scargle plot, GPS L2C, day 127*

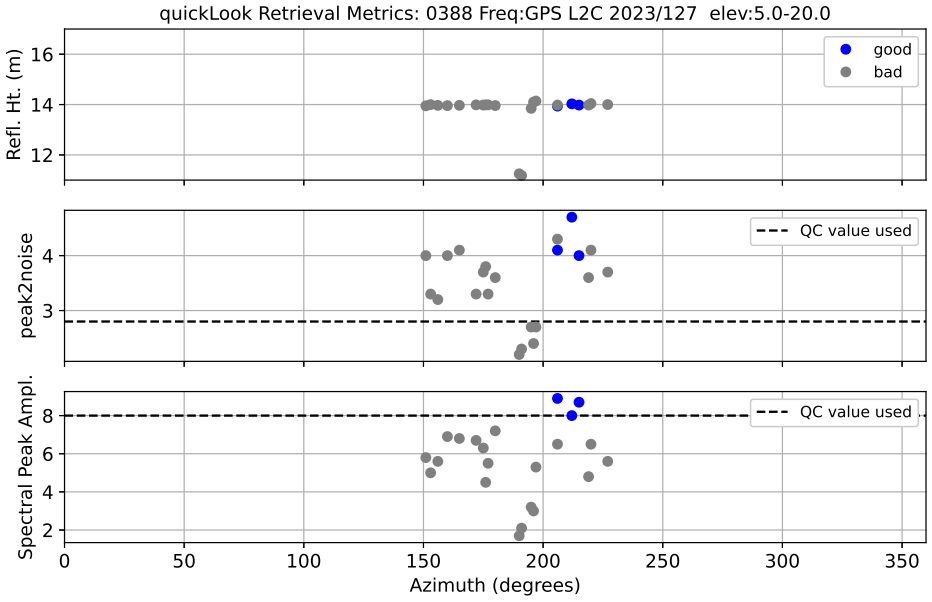

Figure 2.15.: *Spectral quality control parameters, GPS L2C, day 127*

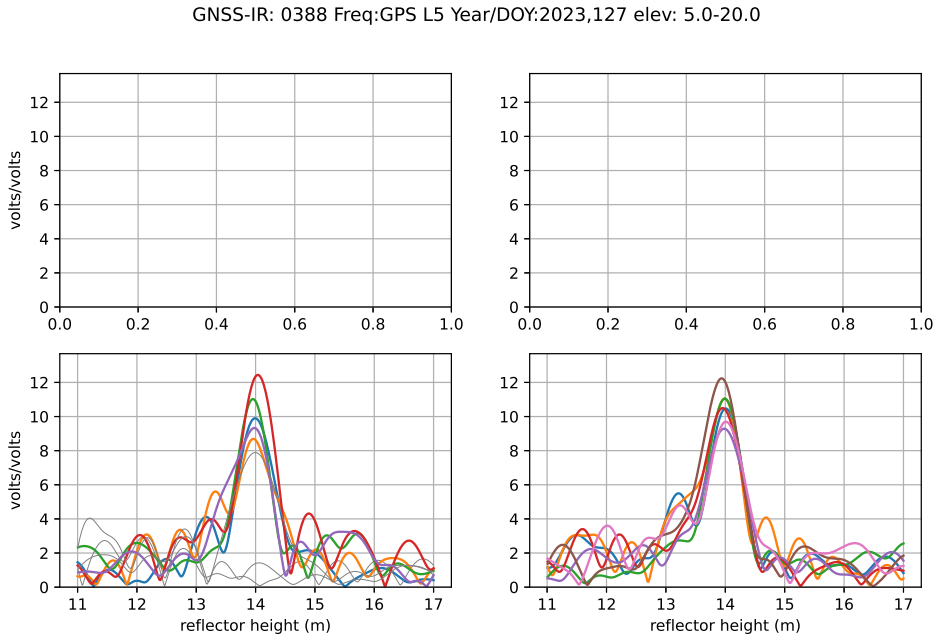

Figure 2.16.: *Lomb-Scargle plot, GPS L5, day 127*

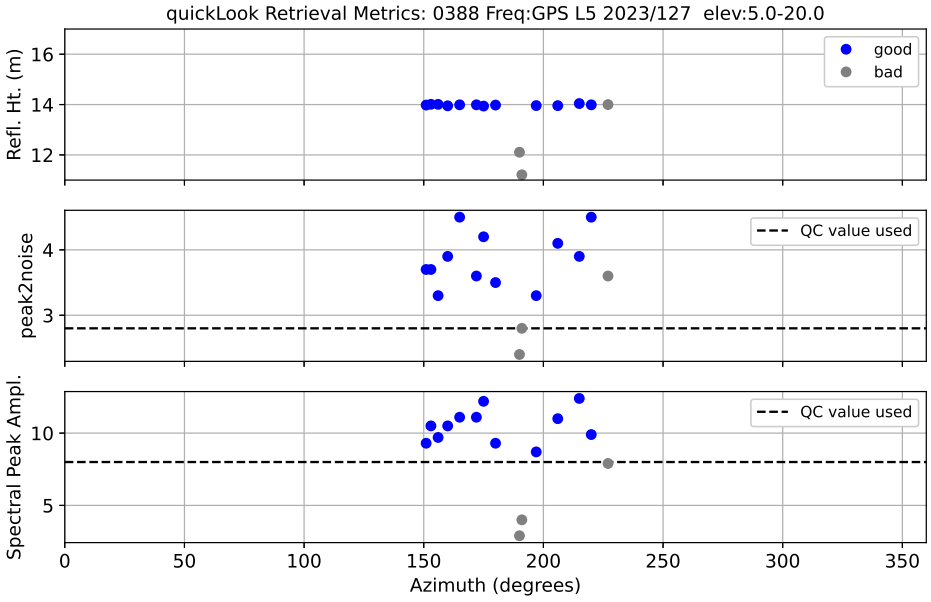

Figure 2.17.: *Spectral quality control parameters, GPS L5, day 127*

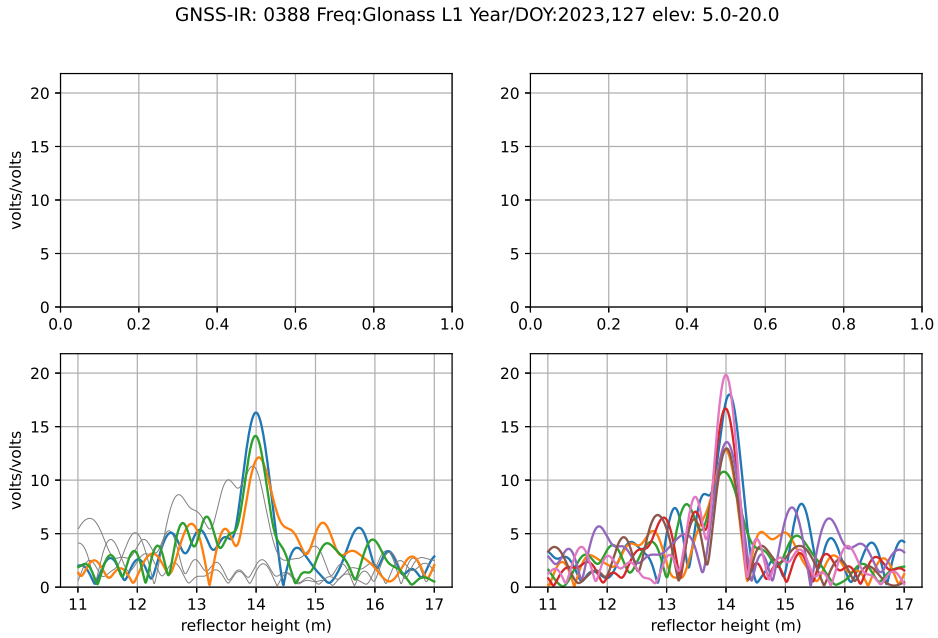

Figure 2.18.: *Lomb-Scargle plot, GLONASS L1, day 127*

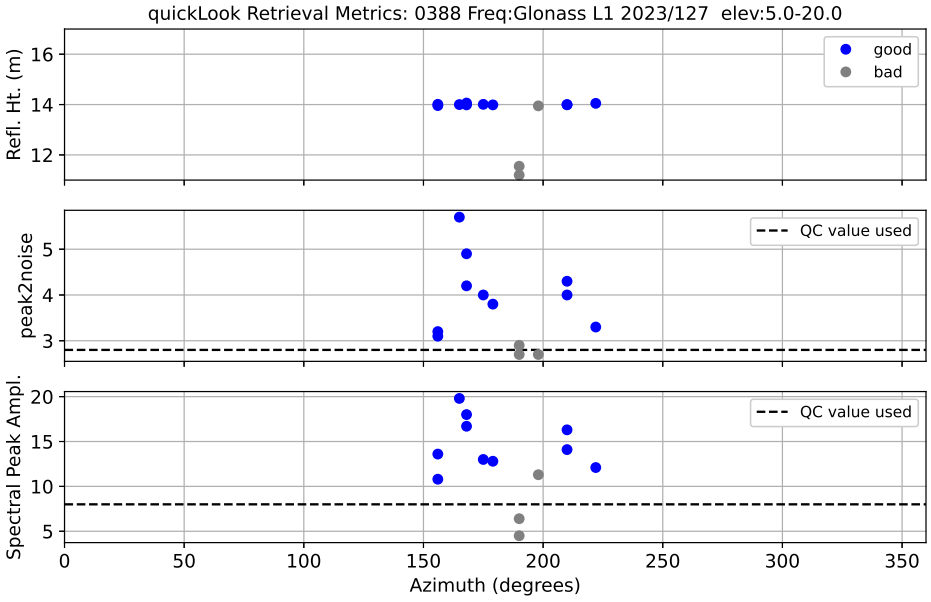

Figure 2.19.: *Spectral quality control parameters, GLONASS L1, day 127*

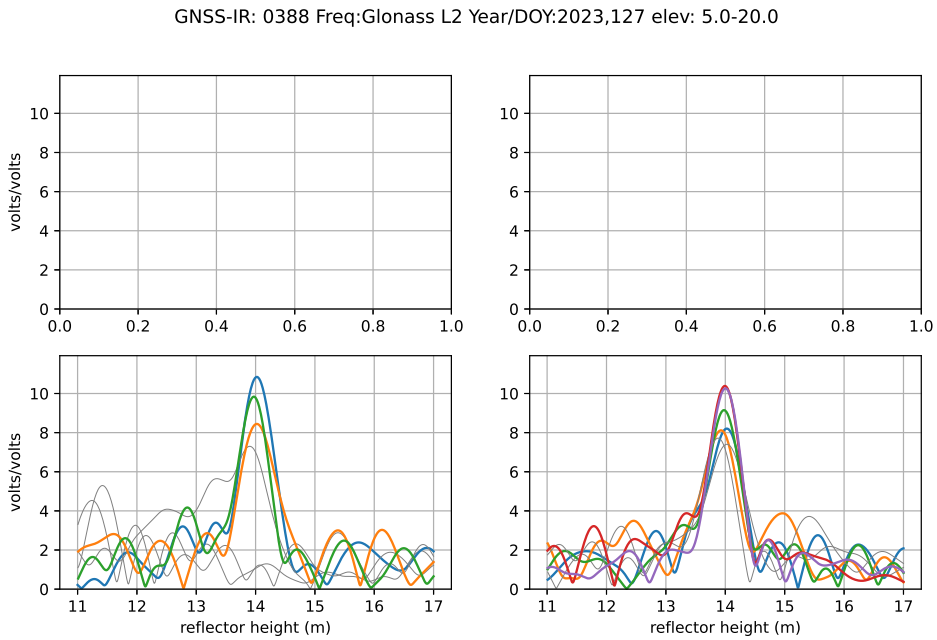

Figure 2.20.: *Lomb-Scargle plot, GLONASS L2, day 127*

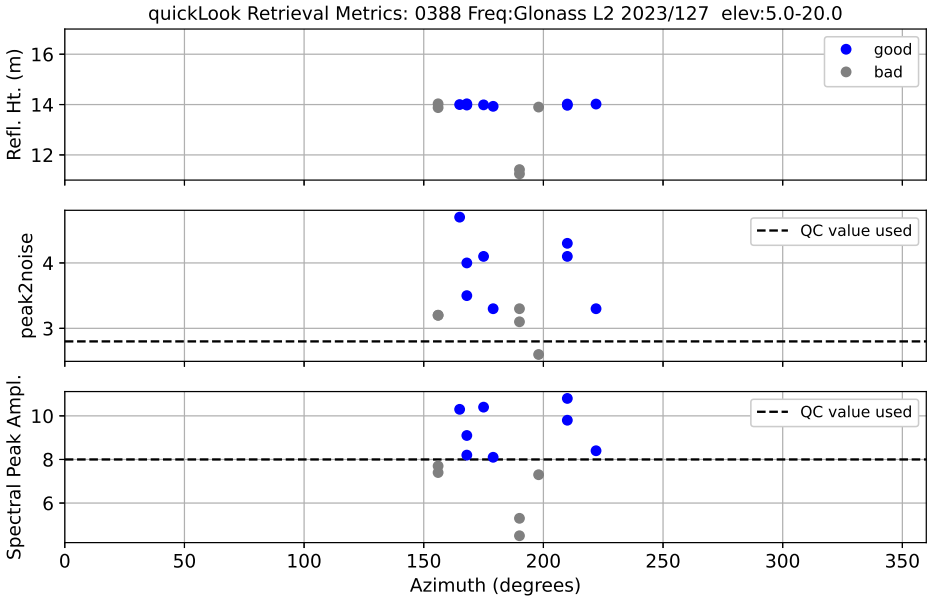

Figure 2.21.: *Spectral quality control parameters, GLONASS L2, day 127*

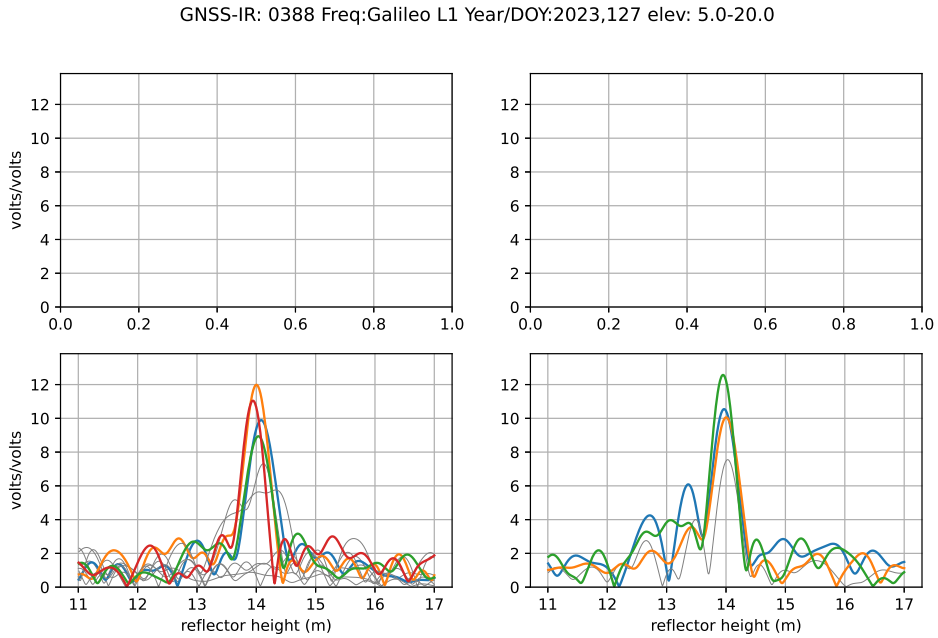

Figure 2.22.: *Lomb-Scargle plot, Galileo E1, day 127*

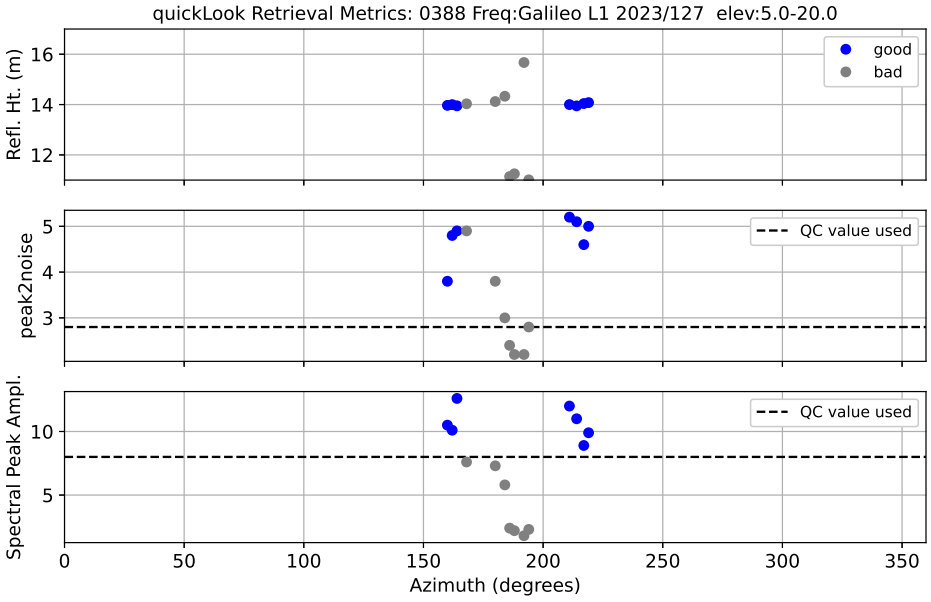

Figure 2.23.: *Spectral quality control parameters, Galileo E1, day 127*

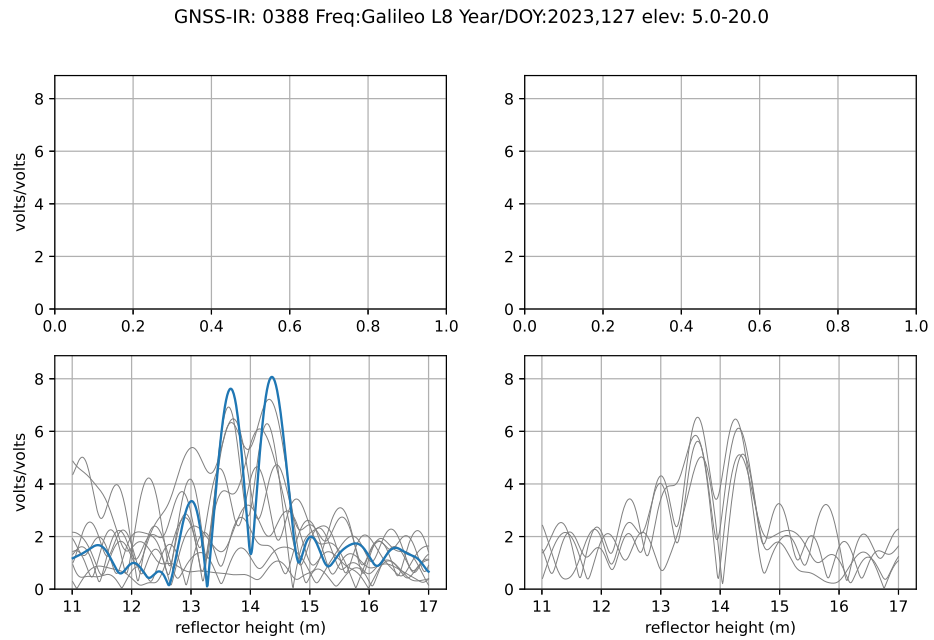

Figure 2.24.: *Lomb-Scargle plot, Galileo E5, day 127*

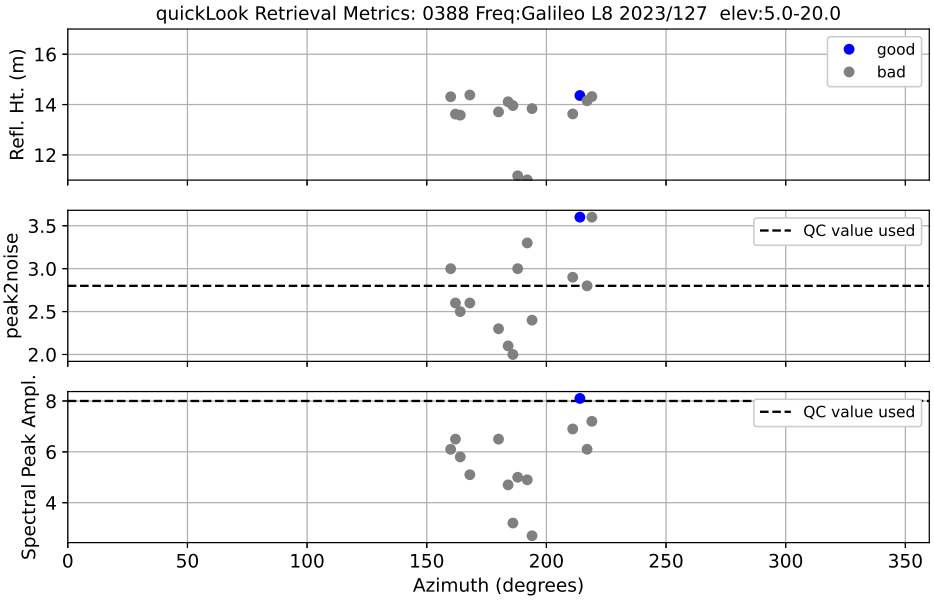

Figure 2.25.: *Spectral quality control parameters, Galileo E5, day 127*

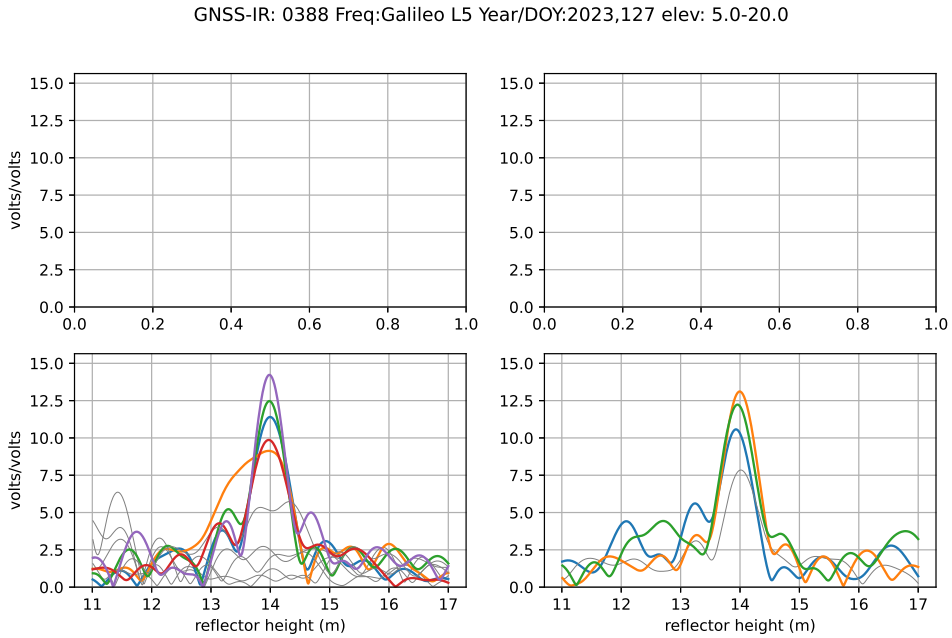

Figure 2.26.: *Lomb-Scargle plot, Galileo E5a, day 127*

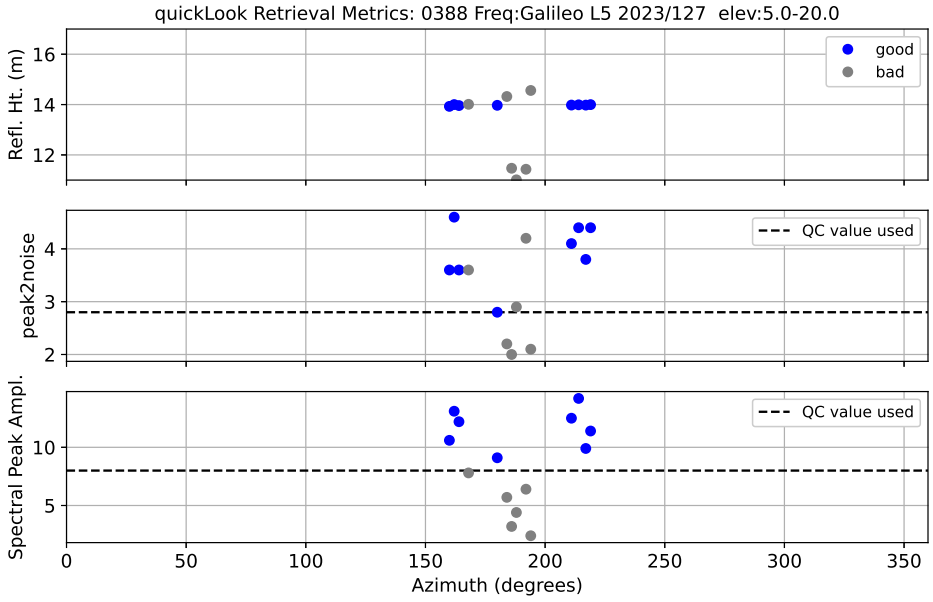

Figure 2.27.: *Spectral quality control parameters, Galileo E5a, day 127*

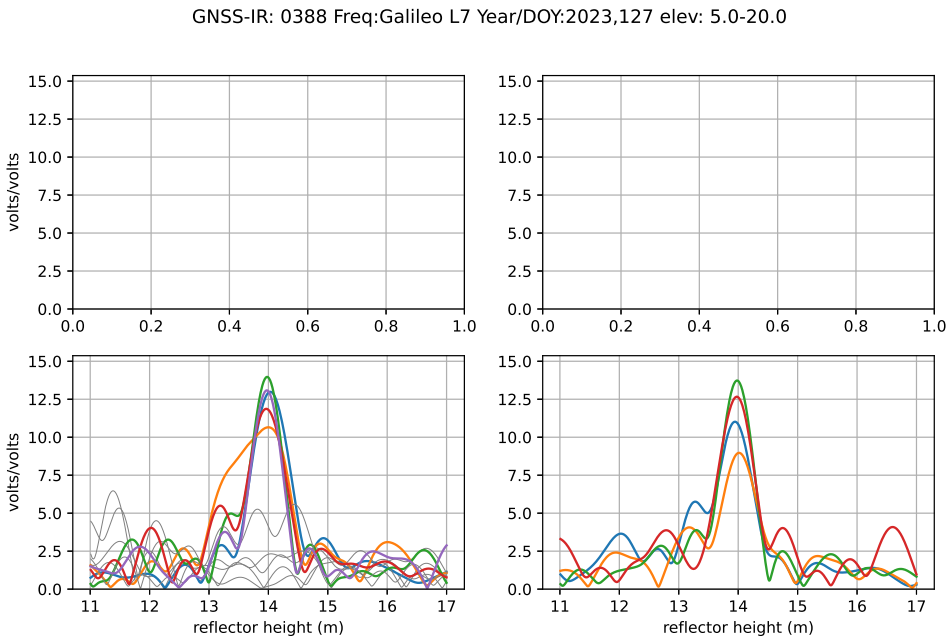

Figure 2.28.: *Lomb-Scargle plot, Galileo E5b, day 127*

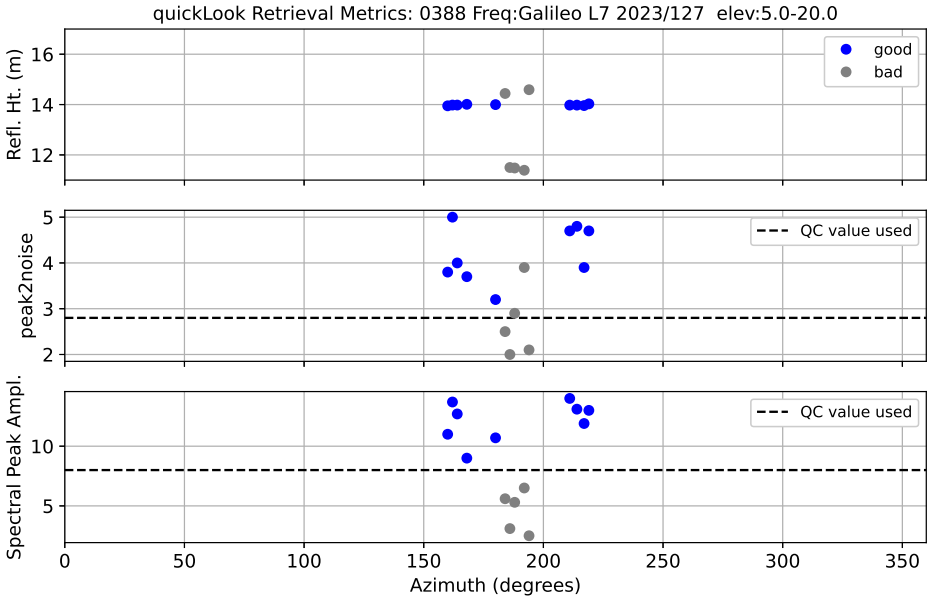

Figure 2.29.: *Spectral quality control parameters, Galileo E5b, day 127*

As depicted above, clear peaks at approximately 14 m are consistently evident in most Lomb-Scargle-plots, concurring to the expected antenna height. However, a notable feature in the quality control plots is the presence of a "hole" representing unaccepted measurements in the data. This observation indicates the presence of the elongated pier at approximately 180 ° to 200 ° azimuth. Due to limitations in the *QuickLook*-module input, the entire azimuth range of 150 ° to 230 ° was plotted, including the pier in the evaluation, thereby explaining the apparent "hole". This observation implies that by lowering the lower height limit to 9 m, the reflections from the pier can be retrieved as well. Since height limits directly correspond to Lomb-Scargle-Periodogram frequency limits, reducing the lower limit allows the reflections from the pier to contribute as a significant spectral peak.

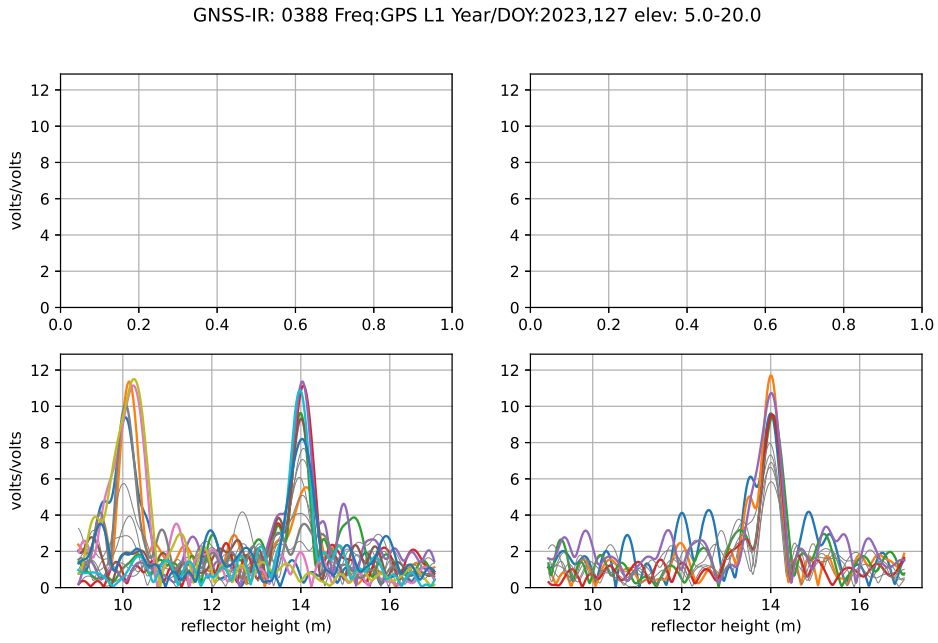

Figure 2.30.: *Lomb-Scargle plot, GPS L1, day 127 with lower h1-limit*

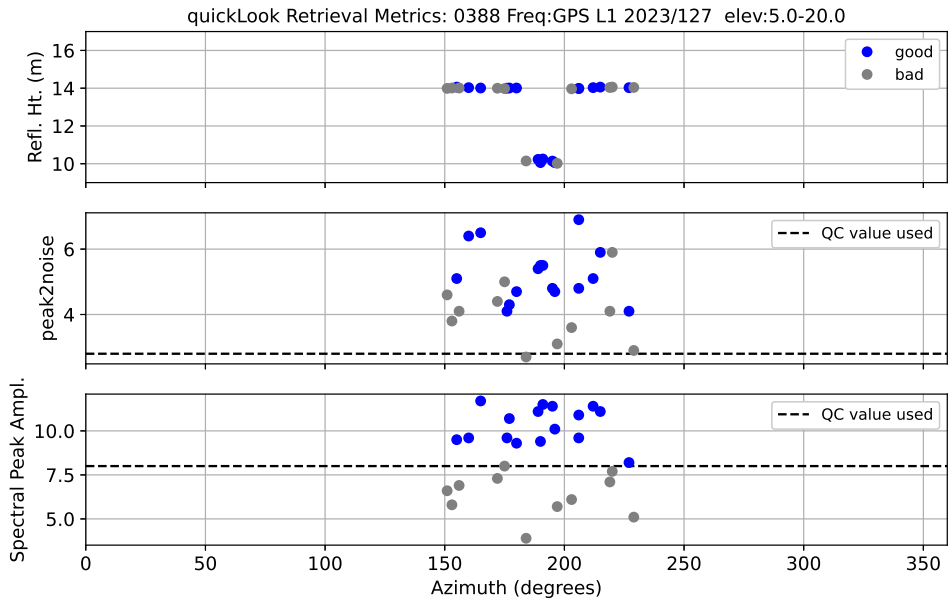

Figure 2.31.: *Quality control parameters, GPS L1, day 127 with lower h1-limit*

Figure 2.30 reveals a significant second peak at approximately 10 m in the south-east quadrant of the Lomb-Scargle plot, originating from reflections of the pier. This observation emphasises the critical importance of considering the physical characteristics of the site and the parameters used to determine spectral peaks through the Lomb-Scargle-Periodogram. Further analysis from the *QuickLook* plots highlights that GPS L2 and L2C frequency retrievals are mostly rejected, especially in the South-Eastern quadrants. As emphasised by Larson (2023b), signals from those frequencies are typically anticipated to yield reliable retrievals. The rejection of those retrievals is likely attributable to the unique characteristics of the SAPOS antenna at the Iffezheim site. Moreover, the Galileo frequencies E6 and E5 at the Iffezheim site either lack data entirely (E6) or contain insufficient and unusable data (E5), as depicted in Figure 2.24. This absence of Galileo E6 data is attributed to the Iffezheim receiver not capturing E6 data, while the behaviour observed in Galileo E5 retrievals can be elucidated by the multipath error envelopes specific to Galileo frequencies. As detailed by Larson (2023a), the Galileo E5 code error demonstrates a distinctive pattern, yielding comparatively smaller code errors. However, for GNSS-IR applications, a larger code error is desirable as it enables the capture of more multipath. Consequently, the Galileo E5 frequency is generally deemed unfeasible for GNSS-IR applications. Nevertheless, most of the other frequencies show promising re-

sults, providing multiple accurate estimations. This indicates that the quality control parameters can be made more stringent, allowing an increase in both the spectral peak amplitude and the peak-to-noise value.

2.4.2. Input-Strategy for Data Analysis

To develop a sensible strategy for data analysis, careful consideration of peak-to-noise and spectral amplitude values is essential to ensure the extraction of the most reliable information for each frequency. Following an evaluation of retrievals from ten different days across all frequencies, the initial parameter for spectral peak amplitude can be set to 8. Despite the presence of some noise in the data, clear peaks for water reflections allow the peak-to-noise ratio to start with a relatively high value of 3. According to Larson (2023a), 2.7 would have been a good starting value for water. This induces that satellite data with peak amplitudes smaller than 8 and peak-to-noise differences smaller than 3 are discarded. This stringent approach ensures the retention of only the most reliable retrievals for the subsequent determination of the vertical distance between the antenna phase centre and the river surface.

The input strategy, defining key parameters for data analysis, is saved and stored in a .json file through the use of the *gnssir_input* command

gnssir_input 0388 -lat 48.8301 -lon 8.1126 -height 185.4264 -h1 11 -h2 17 -peak2noise 3 -ampl 8 -azlist2 150 175 175 185 200 210 210 230 -ellist 10 20 5 12 5 10 10 20 -frlist 1 2 5 101 102 201 205 207

In addition to specifying the station name, position, and spectral parameters, the command includes azimuth and elevation angle lists, as well as a list of frequencies to be considered. The azimuth and elevation angle lists create a mask that corresponds to the expected location of the river surface, ensuring that only reflections from the river are utilised in the analysis (see Table 2.1). This precaution is taken to prevent the inclusion of reflections from other surfaces near the river, which could impact spectral parameters and, consequently, the accuracy of the vertical distance determination. The frequency list is derived from the evaluation of the *QuickLook* retrievals, where the usable frequencies were identified as GPS L1, L2, and L5, GLONASS L1 and L2, and Galileo E1, E5a, and E5b. Notably, the GPS L2C frequency is excluded due to unreliable retrievals, as well as the Galileo E5 frequency.

2.5. Reflector Height Computation

To obtain reflector heights based on the developed input strategy (see Section 2.4.2), the main module of the *gnssrefl* software is executed:

gnssir 0388 2023 1 -doy_end 300

In this command *gnssir* denotes the module, *0388*, *2023* respectively represent the station name and year and *1*, and *doy_end 300* specify the start and end day-of-year of the data set.

The module calculates reflector heights for each spectral peak amplitude of the Lomb-Scargle-Periodograms based on the defined settings. The output consists of 300 text files, each containing data on the vertical distance between the antenna phase centre and the water surface for every satellite pass that has passed the quality control. The stringency of the quality control determines the number of reflector heights, ranging from tens to hundreds, based on the accepted satellite passes. For the evaluation, quality control parameters of 8 for the spectral peak amplitude and 3 for the peak-to-noise ratio were chosen. The results are stored as text files in the following format, exemplified by the data file for day 127 shown in Figure 2.32.

127 - Editor

Datei Bearbeiten Format Ansicht Hilfe

```
% gnssrefl, https://github.com/kristinemlarson, working-on-it
% Phase Center corrections have NOT been applied
% year, doy, RH, sat,UTCtime, Azim, Amp,  eminO, emaxO,NumbOf,freq,rise,EdotF, PkNoise  DelT     MJD    refr-appl
% (1)  (2)   (3) (4)  (5)     (6)   (7)    (8)    (9)   (10)  (11) (12) (13)    (14)     (15)    (16)   (17)
%             m        hrs    deg   v/v    deg    deg  values           hrs                min          1 is yes
 2023 127 14.239   2  9.956 203.65   8.64   5.05  11.95   66   1  1  0.33547   3.32    16.25 60071.414838 1
 2023 127 14.124   3 15.825 221.95   9.14  10.08  19.91   97   1  1  0.62497   4.55    24.00 60071.659363 1
 2023 127 14.124   3 15.825 221.95   9.14  10.08  19.91   97   1  1  0.62497   4.55    24.00 60071.659363 1
 2023 127 14.090   8 17.771 172.00  12.13   5.06  11.95   69   1 -1 -0.35078   3.90    17.00 60071.740440 1
 2023 127 14.045   8 17.810 172.00  12.82   5.06   9.98   50   1 -1 -0.31279   3.09    12.25 60071.742095 1
 2023 127 14.120  10 11.865 163.60  10.30  10.00  19.90   96   1  1  0.61103   4.35    23.75 60071.494352 1
 2023 127 14.035  10 11.600 165.37  15.01   5.00  11.93   71   1  1  0.35748   3.77    17.50 60071.483322 1
 2023 127 13.970  10 11.558 165.37  15.55   5.00   9.90   51   1  1  0.31773   3.13    12.50 60071.481597 1
 2023 127 14.120  10 11.865 163.60  10.30  10.00  19.90   96   1  1  0.61103   4.35    23.75 60071.494352 1
 2023 127 14.155  11  0.277 218.19   9.18  10.08  19.98  106   1 -1 -0.67971   3.76    26.25 60071.011539 1
 2023 127 14.135  11  0.571 215.05  14.49   5.04  11.93   77   1 -1 -0.39094   3.54    19.00 60071.023785 1
 2023 127 14.155  11  0.277 218.19   9.18  10.08  19.98  106   1 -1 -0.67971   3.76    26.25 60071.011539 1
 2023 127 14.159  12  3.277 212.88  16.74   5.00  11.96   70   1  1  0.35204   3.51    17.25 60071.136539 1
 2023 127 14.160  13  4.902 154.77   9.08  10.10  19.96   94   1 -1 -0.60454   3.90    23.25 60071.204248 1
 2023 127 14.160  13  4.902 154.77   9.08  10.10  19.96   94   1 -1 -0.60454   3.90    23.25 60071.204248 1
 2023 127 14.154  14 23.660 158.44   9.42  10.08  19.92  100   1  1  0.64262   4.42    24.75 60071.985845 1
 2023 127 14.005  14 23.381 160.75  10.46   5.03  11.92   74   1  1  0.37546   3.62    18.25 60071.974213 1
 2023 127 14.154  14 23.660 158.44   9.42  10.08  19.92  100   1  1  0.64262   4.42    24.75 60071.985845 1
 2023 127 14.169  15  5.562 178.41   8.49  10.03  19.94   97   1 -1 -0.61813   3.34    24.00 60071.231771 1
 2023 127 14.169  15  5.562 178.41   8.49  10.03  19.94   97   1 -1 -0.61813   3.34    24.00 60071.231771 1
```

Zeile 1, Spalte 1 | 100% | Unix (LF) | UTF-8

Figure 2.32.: *Example text-file for all computed reflector heights (day 127)*

The text file contains relevant data for each computed reflector height corresponding to individual satellites. Noteworthy details include the absence of the phase centre correction at this stage and the application of refraction correction to every satellite. These files serve as a comprehensive record of the computed reflector heights and associated parameters for further analysis.

2.6. Daily Average Computation

To derive a daily average reflector height, the *daily_avg* module is employed, integrating a median filter to mitigate outliers and incorporating the Inter-Frequency-Bias, mapping every signal corresponding to a particular frequency onto the GPS L1 signal, for antenna phase centre-independent heights. Although sub-daily water height variations are to be expected, those values are determined in the *sub_daily* module. For the purpose of exploring the feasibility of GNSS-IR at the SAPOS station in Iffezheim, the daily average values are used. A minimum of 30 accepted satellite data passes is set as a quality control step to ensure meaningful height values. The value of the median filter is determined based on water level variations captured by gauging stations near the SAPOS station, discussed in more detail in Chapter 4. The command syntax is as follows:

daily_avg 0388 0.4 30

Here, *daily_avg* is the module indicator, *0388* represents the station name, *0.4* denotes the median filter (to avoid significant outliers) in m, and *30* specifies the minimum accepted satellite passes for a valid solution.

The module output comprises three text files, providing comprehensive data on final daily reflector heights, contributing factors, and quality control parameters. These results lay the groundwork for subsequent discussions in the following chapter 3.

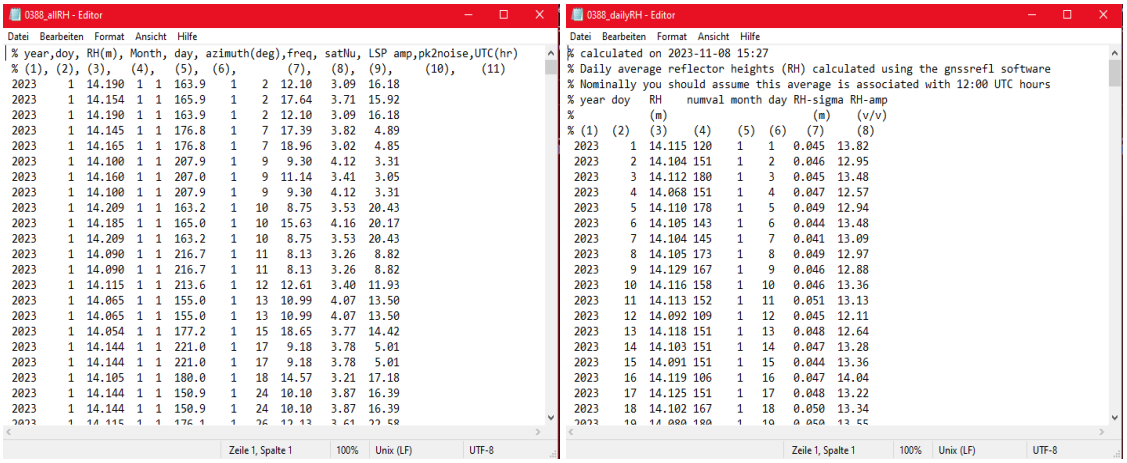

(a) *Example text-file for all computed reflector heights* ***(b)*** *Example text-file for all daily averaged reflector heights*

Figure 2.33.: *Example text-files for the "daily_avg" module*

The text files display the data deriving from the *daily_avg* module. Figure 2.33 contains every corrected and computed reflector height and figure 2.33a only the daily averaged reflector height.

2.7. Corrections

As previously outlined, various corrections are crucial in enhancing the accuracy of GNSS-IR data, specifically the correction of tropospheric delays for sites larger than 10 m. Furthermore for sites with significant tidal ranges the $\dot{H}$-correction is of importance. $\dot{H}$ represents the time varying surface effect, deriving from the change of reflector height $\dot{h}$ and elevation angle $\dot{e}$ during a satellite pass. If a satellite arc is sufficiently short, both $\dot{h}$ and $\dot{e}$ can be assumed to be constants.

2.7.1. Tropospheric Correction

Williams and Nievinski (2017) demonstrated the importance of correcting for tropospheric delay in GNSS-IR applications, stating that the delay is elevation and height dependent. Despite the seeming negligible impact on smaller sites, Williams and Nievinski (2017) recommends correcting for tropospheric delay independent of antenna height. The *gnssrefl* package comprises a straightforward tropospheric zenith delay correction.

2.7.2. Time-varying Surface Effect

The time varying surface effect $\dot{H}$ directly impacts the oscillation frequency (1.8) of the interference pattern. Considering the $\dot{H}$ effect the multipath frequency can be written as

$$f = \frac{2}{\lambda} \cdot (H + \frac{\dot{H} \cdot \tan(e)}{\dot{e}}) \tag{2.18}$$

This causes a shift in the peak of the Lomb-Scargle-Periodogram, deriving from the variations in water level during a single satellite pass. While the $\dot{H}$ correction is not applied for the Iffezheim site due to the assumption of the river being a horizontal planar surface, the *subdaily*-module in the *gnssrefl* software allows for applying corrections for the $\dot{H}$ effect.

2.8. Wind, Waves and other External Influences

The accuracy of GNSS-IR for water level monitoring can also depend on various external influences, especially considering wind and weather causing random roughness on the surface. Random roughness manifests as irregularities on the reflecting surfaces, commonly observed in areas heavily influenced by wind and waves. These irregularities disrupt the coherent reflection of signals, leading to a loss of correlation between transmitted and received signals. The primary consequence of random roughness is the decorrelation of reflected signals. As the reflecting surface undergoes dynamic changes due to wind and wave action, the reflected signals exhibit varying characteristics. This inconsistency impedes the ability to establish a coherent relationship between transmitted and received signals, making the estimation of height infeasible. The inability to estimate height in the presence of random roughness poses a significant challenge to GNSS-IR applications. Sites with pronounced random roughness may not provide reliable data for height determination, necessitating careful consideration of environmental conditions when interpreting GNSS-IR results (Williams, 2023).

2.8.1. Inter-Frequency-Bias

The antenna phase centre is a non-physical point associated with the estimated position in GNSS applications. This point varies for each frequency and antenna,

thereby introducing differences in multi-frequency measurements. In GNSS-IR applications, this implies that the measured heights are frequency (and antenna) dependent. To mitigate this effect, known as the inter-frequency-bias, the *daily_avg* module maps every frequency onto the GPS L1 signal. As described by (Williams, 2023), the inter-frequency-bias can reach values of approximately 10 cm.

Inter-Frequency-Bias in Cold Regions

In cold regions, the freezing of water bodies introduces an additional layer of complexity to IFB considerations. Frozen water exhibits a different Inter-Frequency-Bias compared to its liquid state. Furthermore, the power of signals on ice is notably higher. This disparity in the Inter-Frequency-Bias between water and ice necessitates nuanced adjustments in GNSS-IR methodologies when dealing with frozen water surfaces (Williams, 2023).

3. Results

In the following section 3.1 the results of the previously, in chapter 2, discussed input-parameters for the *gnssrefl* software-package are displayed and evaluated. Since the spectral quality-control is site dependent and needs to be adjusted to the characteristics of the site, two alternative input-strategies are explored and compared to identify a suitable strategy for the data set of the SAPOS station Iffezheim. The strategies are hereafter referred to as:

- **Input 1** for spectral peak amplitude: 8, and a peak-to-noise ratio: 3
- **Input 2** for spectral peak amplitude: 8.3, and a peak-to-noise ratio: 3
- **Input 3** for spectral peak amplitude: 8.5, and a peak-to-noise ratio: 3.4

3.1. Quality-Control: Input 1

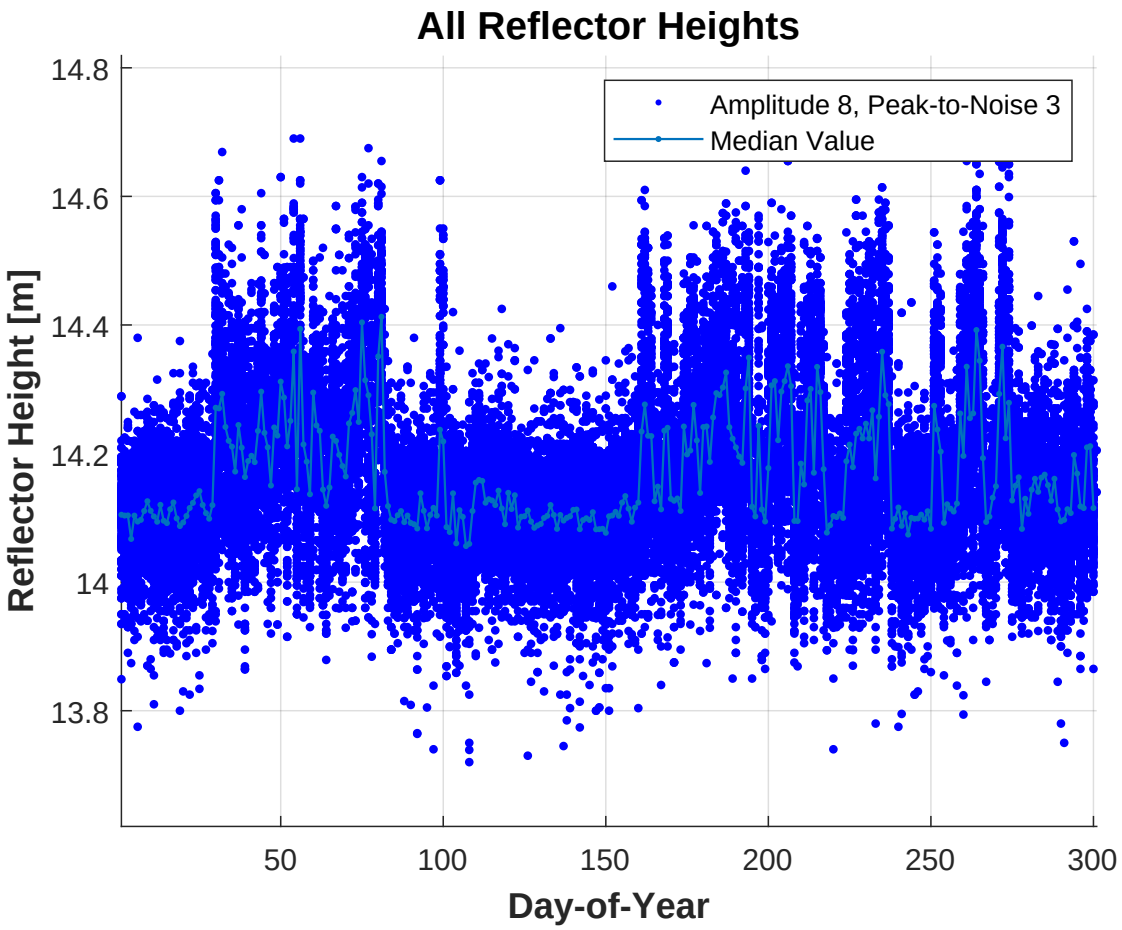

Figure 3.1.: *All reflector heights with median value, quality control: peak amplitude = 8; peak-to-noise = 3*

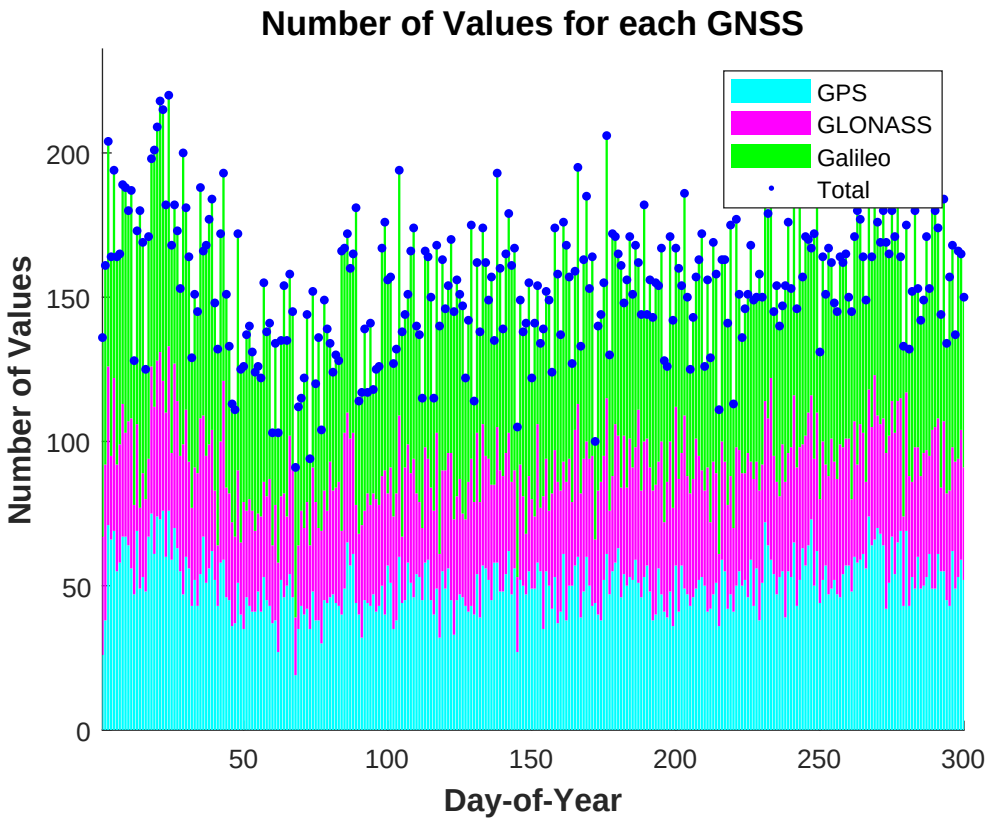

Figure 3.2.: *Number of values that passed the quality control for Input 1*

The results of the first run with quality control settings 8 for spectral peak amplitude and 3 for peak-to-noise ratio as seen in figure 3.1 appear promising. As discussed in section 2.4.1 in chapter 2, the module requires 30 accepted satellite passes and applies a median filter of 0.4 m.
Looking at the number of satellites that passed the quality control in figure 3.2, where a maximum of 226 values on day 233 and a minimum of 91 values on day 68 were observed, **Input 1** seems to work well for the data.
In the subsequent section 3.2 a more stringent quality-control will be deployed to evaluate its impact on the results.

3.2. Quality-Control: Input 2

Input 2 introduces a slight increase in the spectral peak amplitude to 8.3, deriving from the *QuickLook*-plots, discussed in section 2.4.1 of chapter 2.

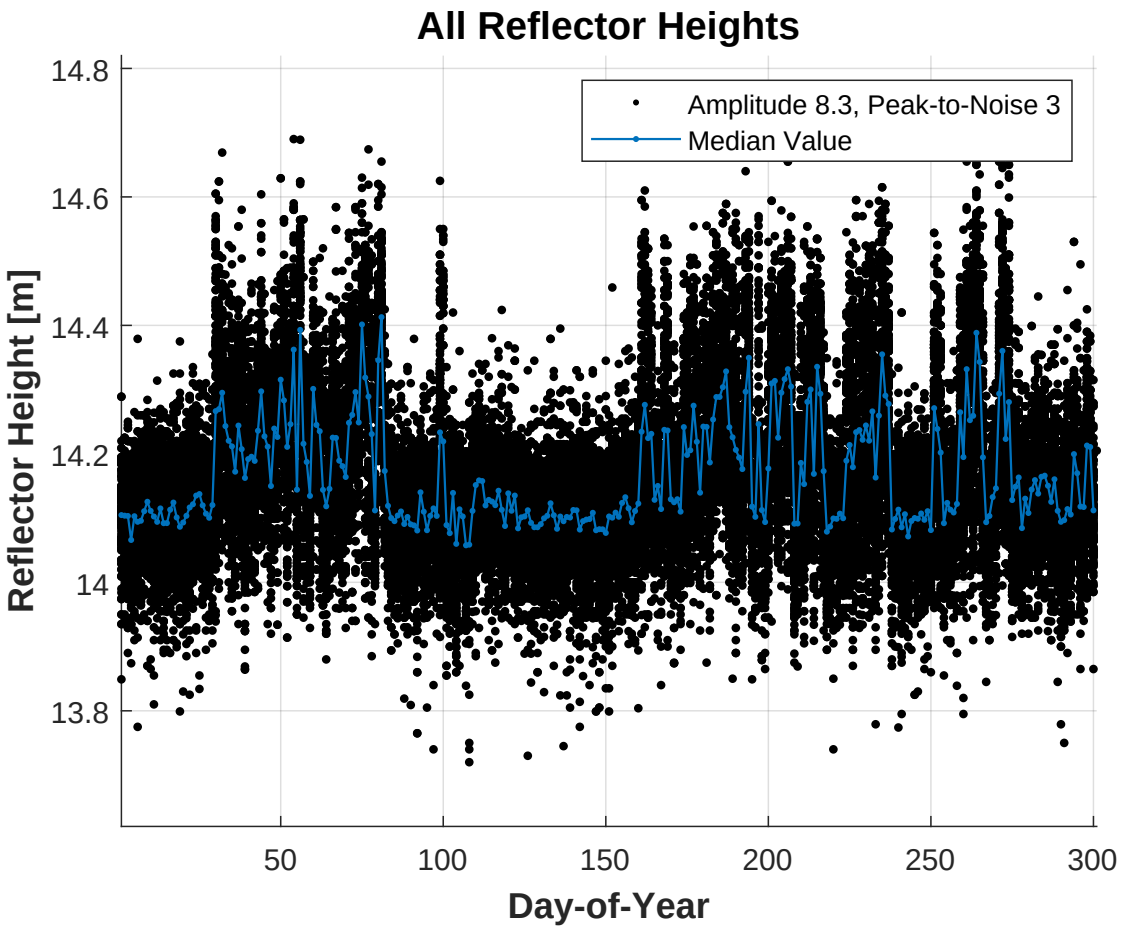

Figure 3.3.: *All reflector heights with median value, quality control: peak amplitude = 8.3; peak-to-noise = 3*

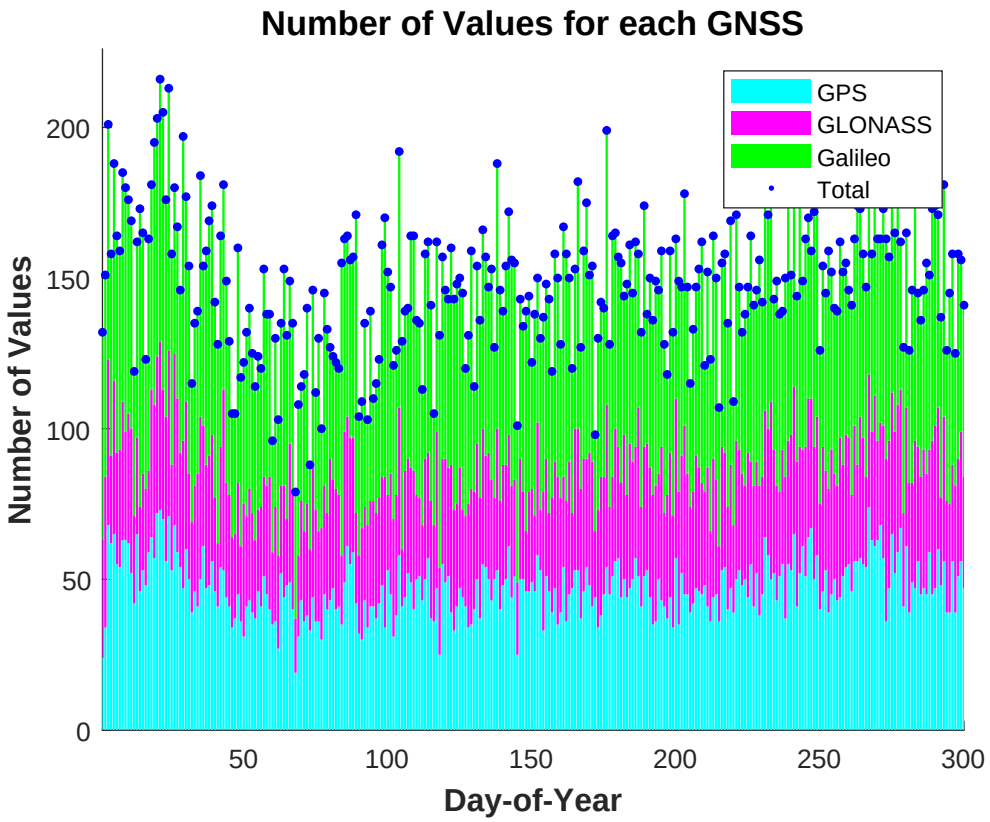

Figure 3.4.: *Number of values that passed the quality control for Input 2*

By implementing the new, more stringent strategy depicted in Figure 3.3, every day successfully passes the quality control. Figure 3.4 shows the number of values passing the quality control, with a maximum of 216 values on day 21 and a minimum of 79 values on day 68. Despite the stricter spectral quality-control limits, there may be still room for adjustment. Therefore, in Section 3.3, the parameters are set even more stringent.

3.3. Quality-Control: Input 3

Input 3 sets the quality-control parameters to a spectral peak amplitude value of 8.5 with a peak-to-noise ratio of 3.4 to get a broader comparison for the data.

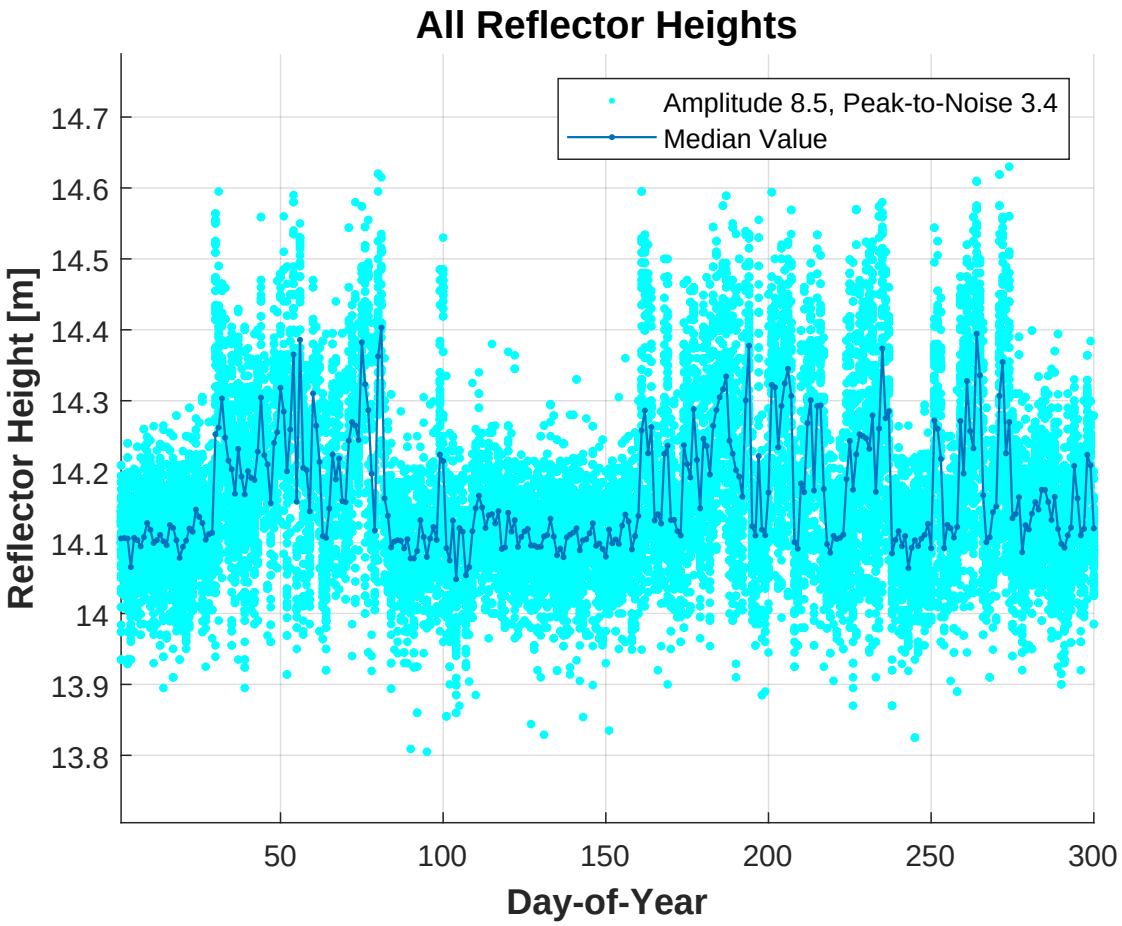

Figure 3.5.: *All reflector heights with median value, quality control: peak amplitude = 8.5; peak-to-noise = 3.4*

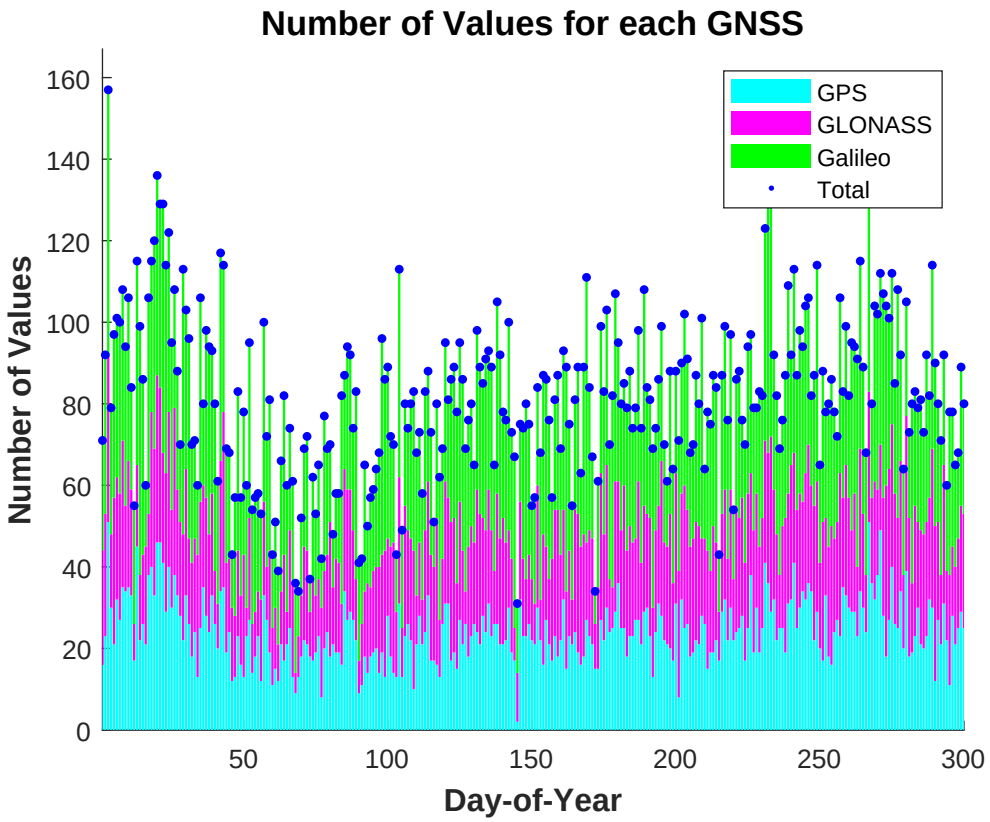

Figure 3.6.: *Number of values that passed the quality control for Input 3*

In Figure 3.6, a notably lower number of values is evident overall. The maximum, reaching 157 values on day 3, and the minimum, dropping to 31 values on day 145, approach the lower limit of the required 30 satellite tracks. This outcome suggests that further tightening the quality-control parameters might lead to a substantial loss of daily averaged data.

3.4. Spectral Input Comparison

A spectral comparison of each strategy is presented hereafter, aiming to identify the best-fitting strategy for the Iffezheim data spanning from January 1, 2023, to October 27, 2023.

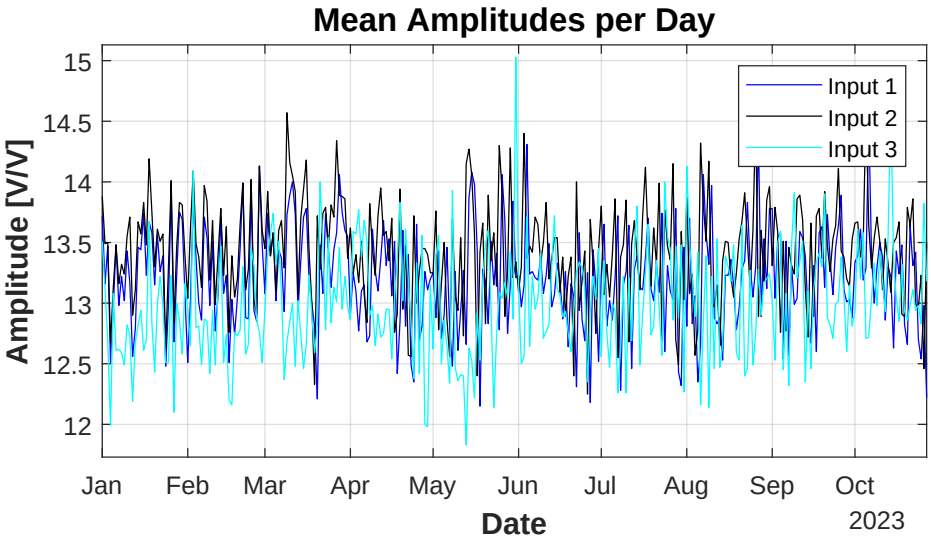

Figure 3.7.: *Comparison of the spectral mean amplitudes*

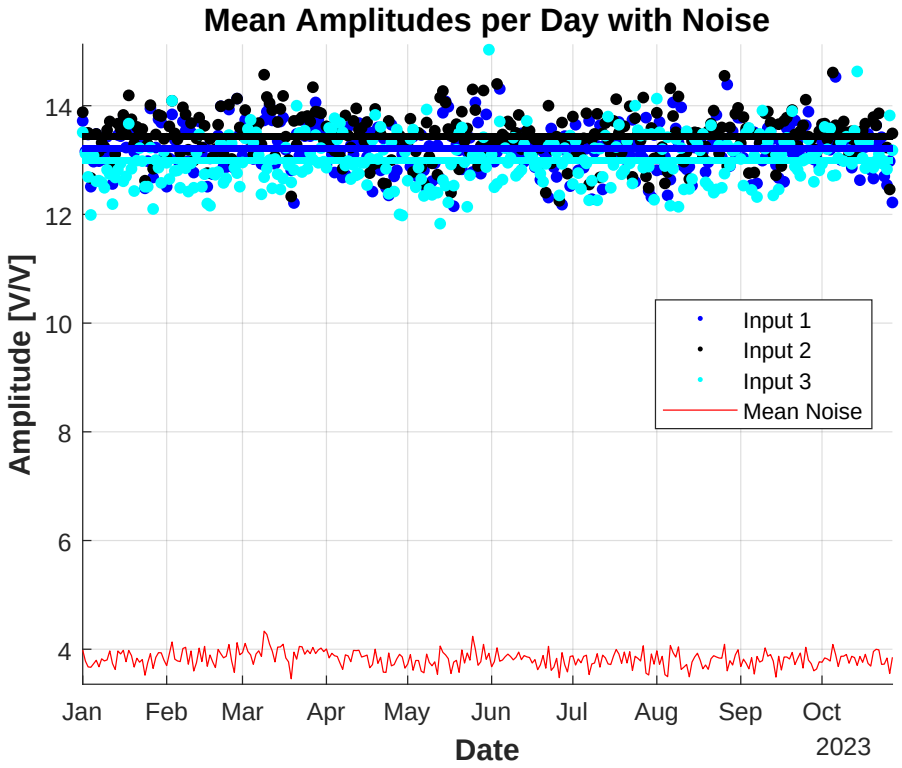

Figure 3.8.: *Comparison of the spectral mean amplitudes with respect to the noise and mean amplitude values over all 300 days*

The analysis of Figure 3.7 and Figure 3.8 indicates that **Input 2** consistently yields the largest spectral peak amplitudes in the Lomb-Scargle-Periodogram, standing out to be the most suitable strategy for the data. Furthermore, Figure 23.8 illustrates the mean amplitudes in relation to the mean noise per day, demonstrating a significant spectral amplitude value for all strategies throughout the entire data set. The mean spectral amplitude-to-noise ratio continuously exceeds a value of 3, as further highlighted in Table 3.1.

Table 3.1.: *Significant spectral amplitude values for each input-strategy*

Input	min. Ampl. [V/V]	max. Ampl. [V/V]
1	12.15 (Day 137)	14.53 (Day 278)
2	12.25 (Day 177)	14.61 (Day 278)
3	11.83 (Day 127)	15.03 (Day 145)
Input	mean Ampl. [V/V]	Amplitude-to-noise [V/V]
1	13.21	3.45
2	13.43	3.51
3	12.99	3.39

Table 3.1 presents key metrics for the spectral peak amplitude, offering a comprehensive comparison of each Input. The table includes minimum, maximum, and mean values for the spectral peak amplitude, as well as the mean amplitude value and the amplitude-to-noise ratio across the entire data set. This summary provides additional clarity, confirming **Input 2** as the best-fit strategy based on these metrics.

3.4.1. Daily Average Reflector Heights and Water Level

Figure 3.9 and Figure 3.10 illustrate the computed daily average reflector heights for all input strategies. These visualisations showcase slight variations in the range of cm, emphasising the impact of different input strategies on the final results. While all strategies follow the same overall trend, differences emerge between them.

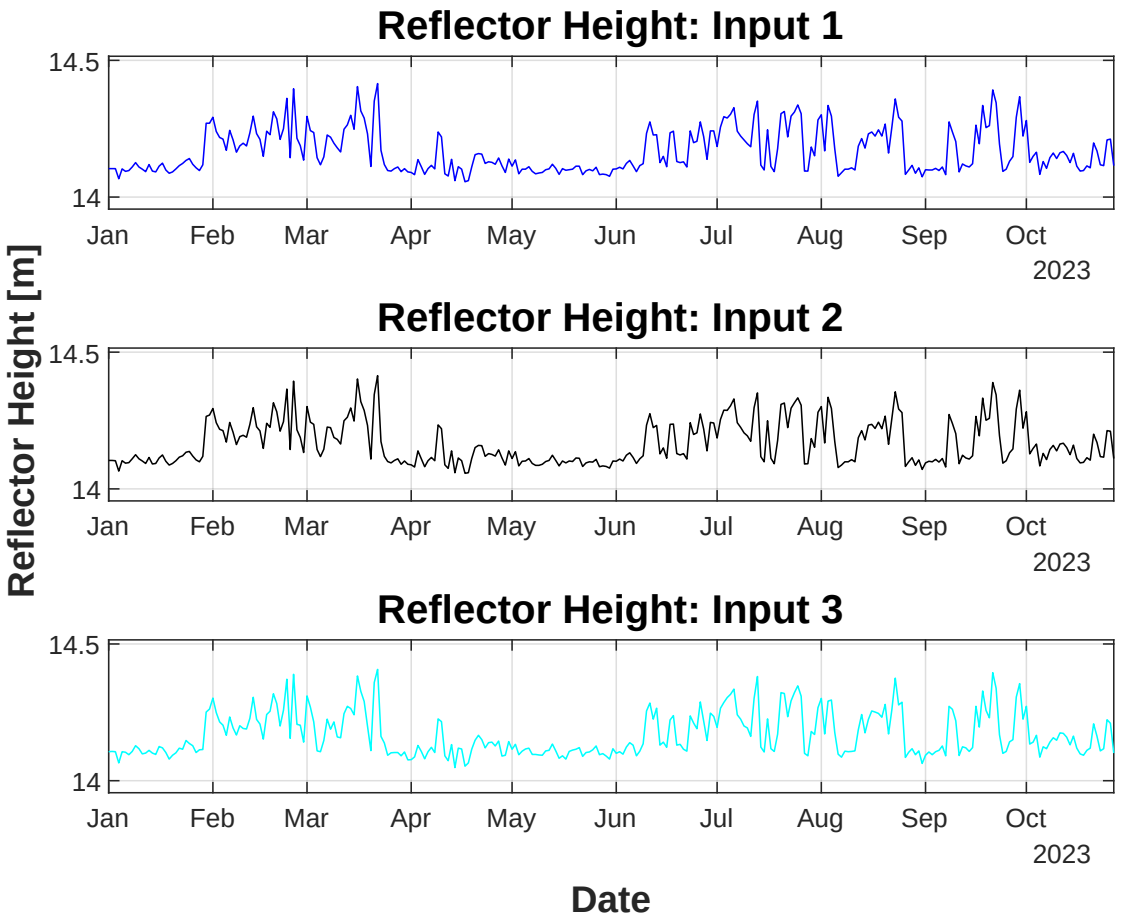

Figure 3.9.: *Daily average results for all inputs*

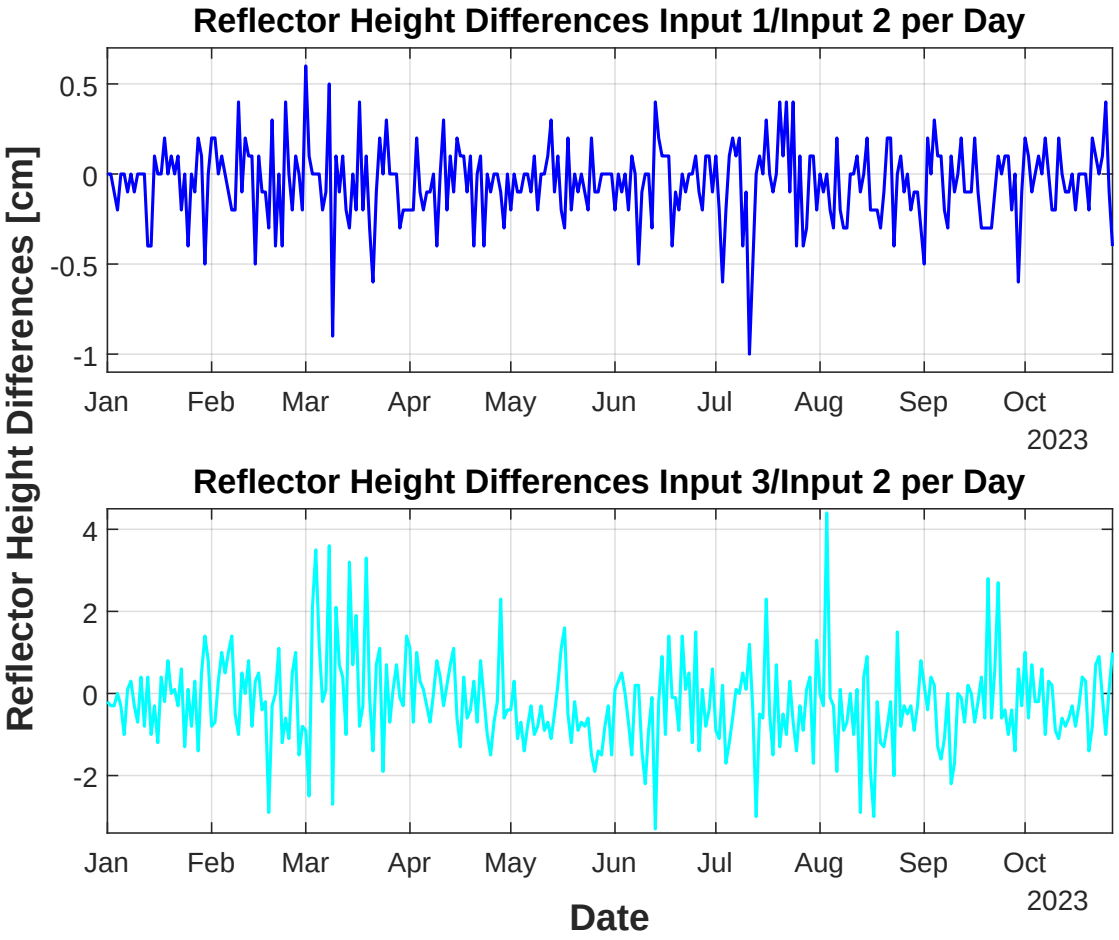

Figure 3.10.: *Daily average differences in contrast to* ***Input 2***

As depicted in Figure 3.10, the variances in daily average reflector heights between **Input 1** and **Input 2** are up to nearly 0.5 cm, while **Input 3** exhibits differences of more than 4 cm. These differences underscore the significance of the chosen quality control parameters in influencing the precision and accuracy of daily average reflector heights.

Using **Input 2** as best-fitting strategy for the data from Iffezheim, the water levels for the year 2023 were computed for all 300 days, ranging from 01. January to 27. October. The daily average reflector height for **Input 2** was applied to the height of the receiver antenna, captured in the RINEX 3.04 files.
Since the water levels in Germany are generally in the DHHN2016 system, it is necessary to convert the ellipsoidal height (ETRS89) given in the RINEX file into the normal height of the DHHN2016 system.

The online tool provided by the Bundesamt für Kartographie und Geodäsie (BKG) (2023) is used for this conversion, according to the formula:

$$H_{\text{DHNN2016}} = h_{\text{ETRS}} - \xi_{\text{GCG2016}} = 137.374\,\text{m} \tag{3.1}$$

The obtained water levels are depicted in figure 3.11.

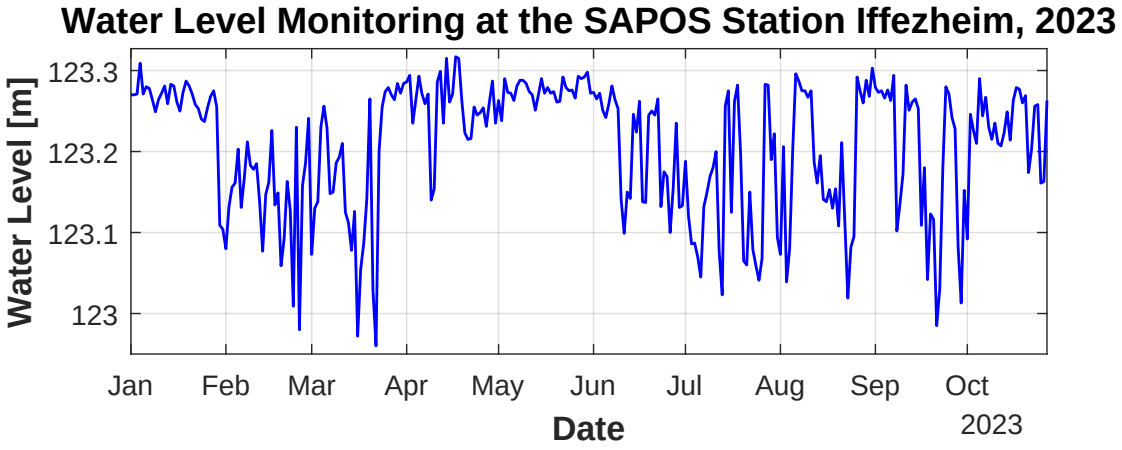

Figure 3.11.: *Water level, SAPOS station Iffezheim, 01. January 2023 - 27. October 2023*

The water level reached its minimum of 122.93 m on February 25th and its maximum of 123.31 m on April 18th, showing variations in water height of up to 0.39 m. These results provide insights into the dynamic changes in water levels over the monitoring period and are further evaluated in section 3.5.

3.5. GNSS-IR and Gauge Data Comparison

To assess the reliability of the GNSS-IR data from the SAPOS station in Iffezheim, comparisons were made with gauge data from the Iffezheim and Kehl stations, both situated along the river. The Iffezheim gauge is located approximately 2.5 km north of the sluice on river kilometre-marker 336.201, while the Kehl gauge is situated to the south of Iffezheim at kilometre-marker 292.245.

(a) *Location of the gauge in Iffezheim* ***(b)*** *Location of the gauge in Kehl*

Figure 3.12.: *Locations of the gauging stations Iffezheim and Kehl, relative to the SAPOS station*

Figure 3.12 depicts the locations of the gauging stations Iffezheim and Kehl, relative to the SAPOS station on the sluice in Iffezheim on Google Earth. A Comparison of the data gathered at the gauging stations and the SAPOS station is shown in figure 3.13 and figure 3.14.

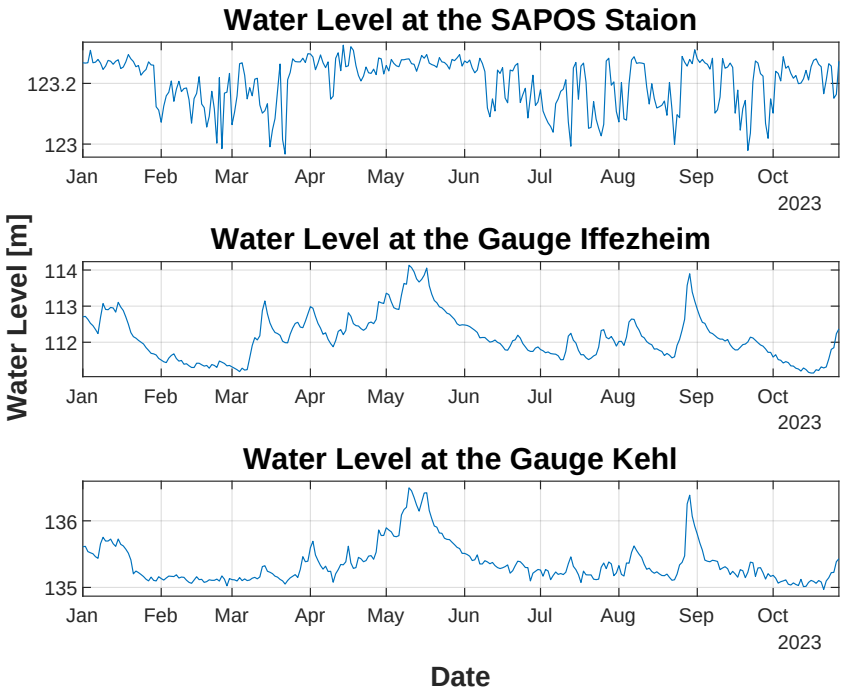

Figure 3.13.: *Water levels of gauge and GNSS-IR results, daily average 2023*

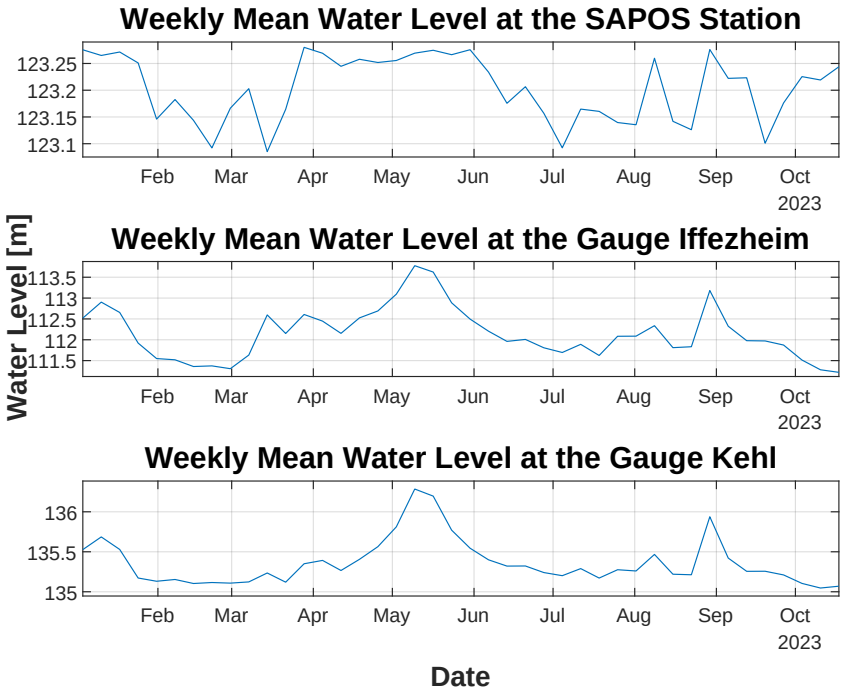

Figure 3.14.: *Water levels of gauge and GNSS-IR results, weekly average 2023*

In Figure 3.13, daily averaged data from the gauge stations Iffezheim and Kehl are plotted alongside the daily averaged data from the **Input 2** results. To provide a broader perspective on water level variations, figure 3.14 displays the results as weekly averages. Notably, the gauge data from Iffezheim and Kehl exhibit a similar overall trend, but they differ significantly in the range of water level variations. While Iffezheim shows variations of 1 m to 1.5 m, Kehl experiences fluctuations exceeding 2 m. In contrast, the SAPOS station data indicates more modest variations, staying below 0.5 m. Moreover, the trends at the SAPOS station differ from those observed at the gauge stations. These outcomes will be further explored and interpreted in the subsequent chapter 4.

4. Conclusion

In summary, the GNSS-IR-based water level monitoring conducted at the SAPOS station in Iffezheim reveals distinct differences compared to traditional gauge data. The location of the SAPOS station on top of the sluice (see 2.2 and 2.1) introduces complexities due to frequent ship passages through the area of the Fresnel zones and water level changes caused by the sluice operations, impacting the accuracy of GNSS-IR measurements and therefore explaining the differences to the gauge data partly. Nevertheless, despite promising outcomes observed within the site evaluation using the *gnssrefl* software by Prof. Larson, the comparison with real gauge data indicates that employing water level monitoring through GNSS-IR is not feasible at the Iffezheim site. The GNSS-IR data only captures slight trends in water level changes over an extended time period and demonstrates low correlation with the gauge data, slightly higher in weekly mean values, than for the daily data. The correlations (shown in table 4.1 and 4.2) between the GNSS-IR data and gauges Iffezheim and Kehl are significantly weaker than the correlation between the gauges themselves, indicating the influence of the specific site characteristics.

Table 4.1.: *Correlations of Daily Gauge Data and GNSS-IR Measurements*

Correlation	GNSS-IR	Gauge Iffezheim	Gauge Kehl
GNSS-IR	1	0.4425	0.4350
Gauge Iffezheim	0.4425	1	0.9206
Gauge Kehl	0.4350	0.9206	1

Table 4.2.: *Correlations of Weekly Gauge Data and GNSS-IR Measurements*

Correlation	GNSS-IR	Gauge Iffezheim	Gauge Kehl
GNSS-IR	1	0.5835	0.5965
Gauge Iffezheim	0.5835	1	0.9344
Gauge Kehl	0.5965	0.9344	1

Table 4.1 and table 4.2 both verify a strong correlation of the data between Iffezheim and Kehl, although they lay over 35 km apart from each other. The correlations between the gauges and the GNSS-IR data are as mentioned significantly lower, further supporting the in-applicability of GNSS-IR at the site in Iffezheim.

In conclusion, this study emphasises that water level monitoring through GNSS-IR at the Iffezheim site is unfeasible. Nonetheless, the applicability of this method to SAPOS stations in general may vary based on site-specific conditions, necessitating further research for comprehensive validation. Despite the challenges posed by the Iffezheim SAPOS station, such as the presence of a sluice, ship passages, and narrow reflection zones, GNSS-IR could still prove functional at other SAPOS stations with more suitable locations. Given that the multipath effect required for GNSS-IR is typically considered undesirable, most GNSS receivers at SAPOS stations avoid water surfaces in their near environment, however low-cost GNSS receivers can instead be utilised to establish water level monitoring stations. This approach, supported by other GNSS-IR researchers (Fagundes et al., 2021; Karegar et al., 2022), showcases the cost-effectiveness and accessibility of GNSS-IR as an innovative method for water level monitoring, instead of traditional gauges. To further contribute to the field, a self-constructed low cost GNSS receiver designed for GNSS-IR purposes is presented in the thesis's appendix, underlining the ongoing efforts to enhance and expand GNSS-IR applications for water level monitoring.

Appendix

Appendix A.

Low cost GNSS receiver build

To validate measurements and facilitate the use of GNSS-IR for water level monitoring, a low-cost GNSS receiver was constructed. This construction is solely presented as contribution to the GNSS-IR community emphasising the ongoing exploration of cost-effective alternatives for water level monitoring, completely independent from the prior analysis of the SAPOS station. The receiver was assembled using the *Qwiic* connect system by *SparkFun*, which employs 4-pin JST connectors to quickly interface development boards with sensors over the I2C bus. The final build consists of the following components:

1. *SparkFun Qwiic Pro Micro USB-C (ATmega32U4)*
2. *SparkFun GPS NEO-M9N*
3. *Ublox GNSS Multi-band antenna*
4. *SparkFun Qwiic OpenLog with 32 Gb SD-card*
5. *SparkFun Sunny Buddy Solar Charger V13*
6. *6600 mAh, 3.7 V LiPo Battery*
7. *6W Solar Panel*

The *Qwiic Pro Micro* serves as the development board due to its compact size, USB functionality, and *ATmega32U4* microcontroller, making it well-suited for a low-cost GNSS system. The *SparkFun GPS NEO-M9N* Breakout with SMA is used to capture GPS, GLONASS, and Galileo data required for GNSS-IR. A *GNSS Multi-band antenna* is connected to the SMA connector to capture a broad range of frequencies. All received data are stored in NMEA format on a *32Gb SD card* inserted into the *SparkFun Qwiic OpenLog*. Power is supplied through a *solar panel* and a *6600mAh LiPo battery* connected to the *SparkFun Sunny Buddy Solar Charger V13*. All components are connected with *Qwiic* cables, and the *solar panel* is connected via a barrel jack and USB serial interface. The total cost of the system is approximately 253 Euros. The constructed system is depicted in Figure A.1.

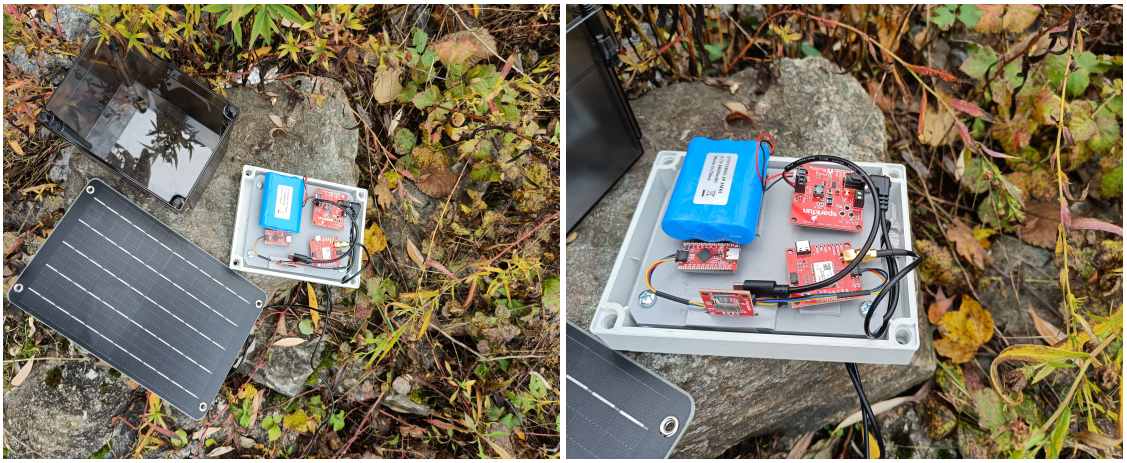

Figure A.1.: *SparkFun self-constructed GNSS receiver*

To program the micro-controller the Arduino IDE 2.2.1 was utilised. The Code powering the NMEA-measurements is provided below.

```
#include <Wire.h> //Needed for I2C to GPS

#include "SparkFun_Ublox_Arduino_Library.h"
SFE_UBLOX_GPS myGNSS;

#include "SparkFun_Qwiic_OpenLog_Arduino_Library.h"

//Create instance
OpenLog myLog;
//Status LED connected to digital pin 13
int ledPin = LED_BUILTIN;
//Default Qwiic OpenLog I2C address
const byte OpenLogAddress = 42;

#define BUFFER_SIZE 100
char nmeaBuffer[BUFFER_SIZE];
int bufferIndex = 0;


String currentDate; //current Date for log files

void setup()
{
```

```
24    pinMode(ledPin, OUTPUT);
25  //Serial.begin(115200);
26  //set Baudrate to 115200 for serial monitor
27
28    Wire.begin(); //Initialize the I2C
29    myLog.begin(); //Initialize the Log
30
31    //Check if NEO-M9N is ready
32    if (myGNSS.begin() == false)
33    {
34      //Wait for NEO-M9N
35      while (1);
36    }
37
38    //Enable NMEA Senteces
39    myGNSS.enableNMEAMessage(UBX_NMEA_GLL, COM_PORT_I2C);
40    myGNSS.enableNMEAMessage(UBX_NMEA_GSA, COM_PORT_I2C);
41    myGNSS.enableNMEAMessage(UBX_NMEA_GSV, COM_PORT_I2C);
42    myGNSS.enableNMEAMessage(UBX_NMEA_RMC, COM_PORT_I2C);
43    myGNSS.enableNMEAMessage(UBX_NMEA_GGA, COM_PORT_I2C);
44    myGNSS.enableNMEAMessage(UBX_NMEA_VTG, COM_PORT_I2C);
45    //1Hz update rate is sufficient for GNSS-IR
46    myGNSS.setNavigationFrequency(1);
47    myGNSS.saveConfiguration();
48  }
49
50  void loop()
51  {
52    //See if new data is available.
53    //Process bytes as they come in.
54    myGNSS.checkUblox();
55    delay(250); //don't pound to hard on I2C
56    //Check Date for log file
57    currentDate = getCurrentDate();
58  }
59
60  void SFE_UBLOX_GPS::processNMEA(char incoming)
61  {
62    //Take the incoming char from the Ublox I2C port
63    //and write in nmeaBuffer
```

```
64    if (incoming == '\n') {
65      //If \n ist reached pass the Buffer to OpenLog
66      //and clear Buffer for next Sentence
67      //add nullbyte to create c-string
68      nmeaBuffer[bufferIndex] = '\0';
69      //Create new Logfile for each day /
70      //append to log file (.append creates file)
71      if (currentDate.length() > 0) {
72        String filename = currentDate + ".txt";
73        myLog.append(filename);
74        myLog.println(nmeaBuffer);
75      }
76 //Serial.println(nmeaBuffer);
77      bufferIndex = 0; // clear Buffer
78    } else {
79      //Add char to Buffer
80      if (bufferIndex < BUFFER_SIZE - 1) {
81        nmeaBuffer[bufferIndex++] = incoming;
82      }
83    }
84 }
85
86 String getCurrentDate()
87 {
88    uint8_t day = myGNSS.getDay();
89    uint8_t month = myGNSS.getMonth();
90    uint16_t year = myGNSS.getYear();
91    String currentDate = String(day) +
92    String(month) + String(year);
93    return currentDate;
94 }
```

The system, executing the provided source code, successfully collected NMEA data over several days at a test site. However, due to time constraints, water level measurements using the system have not been conducted as of now.

Bibliography

Axelrad, P., Larson, K. M., & Jones, B. (2005). Use of the correct satellite repeat period to characterize and reduce site-specific multipath errors, In *Proceedings of the 18th international technical meeting of the satellite division of the institute of navigation (ion gnss 2005)*.

Bilich, A., & Larson, K. M. (2007). Correction published 29 March 2008: Mapping the GPS multipath environment using the signal-to-noise ratio (SNR). *Radio Science*, *42*(06), 1–16.

Bundesamt für Kartographie und Geodäsie (BKG). (2023). GCG2016 [[Last Call: 03.12.2023]]. https://gibs.bkg.bund.de/geoid/gserlaeuter_g.php

Collins, J. (2001). *Assessment and development of a tropospheric delay model for aircraft users of the global positioning system*. National Library of Canada= Bibliothèque nationale du Canada, Ottawa.

Fagundes, M. A. R., Mendonça-Tinti, I., Iescheck, A. L., Akos, D. M., & Geremia-Nievinski, F. (2021). An open-source low-cost sensor for snr-based gnss reflectometry: Design and long-term validation towards sea-level altimetry. *GPS Solutions*, *25*(2), 73.

Garrison, J. L., Katzberg, S. J., & Hill, M. I. (1998). Effect of sea roughness on bistatically scattered range coded signals from the Global Positioning System. *Geophysical research letters*, *25*(13), 2257–2260.

Georgiadou, Y., & Kleusberg, A. (1988). On carrier signal multipath effects in relative gps positioning. *Manuscripta geodaetica*, *13*(3), 172–179.

Hall, C., & Cordey, R. (1988). Multistatic Scatterometry, In *International Geoscience and Remote Sensing Symposium, 'Remote Sensing: Moving Toward the 21st Century'*. https://doi.org/10.1109/IGARSS.1988.570200

Hristov, H. (2000). *Fresnel zones in wireless links, zone plate lenses and antennas*. Artech House.

International GNSS Service (IGS),RINEX Working Group and Radio Technical Commission for Maritime Services Special Committee 104 (RTCM-SC104). (2018). Rinex - the receiver independent exchange format [[Online; Stand 23. November 2018]]. http://acc.igs.org/misc/rinex304.pdf

J. Sanz Subirana, J. J. Z., & Hernández-Pajares, M. (2011a). Ionospheric delay. https://gssc.esa.int/navipedia/index.php?title=Ionospheric_Delay

J. Sanz Subirana, J. J. Z., & Hernández-Pajares, M. (2011b). Tropospheric delay. https://gssc.esa.int/navipedia/index.php?title=Tropospheric_Delay

Karegar, M. A., Kusche, J., Geremia-Nievinski, F., & Larson, K. M. (2022). Raspberry pi reflector (rpr): A low-cost water-level monitoring system based on gnss interferometric reflectometry [e2021WR031713 2021WR031713]. *Water Resources Research*, *58*(12). https://doi.org/https://doi.org/10.1029/2021WR031713

Klobuchar, J. A. (1983). *Ionospheric effects on Earth-space propagation* (Vol. 84). Ionospheric Physics Division, Air Force Geophysics Laboratory.

Komjathy, A., Maslanik, J., Zavorotny, V. U., Axelrad, P., & Katzberg, S. J. (2000). Sea ice remote sensing using surface reflected gps signals, In *IGARSS 2000. IEEE 2000 International Geoscience and Remote Sensing Symposium. Taking the Pulse of the Planet: The Role of Remote Sensing in Managing the Environment. Proceedings (Cat. No. 00CH37120)*. IEEE.

Langley, R. B., Teunissen, P. J., & Montenbruck, O. (2017). Introduction to GNSS. In *Springer handbook of global navigation satellite systems* (pp. 3–23). Springer International Publishing. https://doi.org/10.1007/978-3-319-42928-1_1

Larson, K. M. (2023a). gnssrefl Documentation [[Online: Revision 0b3c0e99]]. https://gnssrefl.readthedocs.io/en/latest/index.html

Larson, K. M., Löfgren, J. S., & Haas, R. (2013). Coastal sea level measurements using a single geodetic GPS receiver. *Adv. Space Res.*, *51*, 1301–1310.

Larson, K. M., Williams, S., Dittmann, T., Enloe, K., Nylen, T., Nievinski, F., & Purnell, D. (2023). 2023 gnss interferometric reflectometry short course [https://www.earthscope.org/event/2023-gnss-ir-short-course/].

Larson, K. M. (2023b). GNSS Interferometric Reflectometry [[Online; Stand 21. August 2023]]. https://gnss-reflections.org/overview

Larson, K. M., & Nievinski, F. G. (2013). GPS snow sensing: results from the EarthScope Plate Boundary Observatory. *GPS solutions*, *17*, 41–52.

Larson, K. M., Ray, R. D., Nievinski, F. G., & Freymueller, J. T. (2013). The accidental tide gauge: A gps reflection case study from kachemak bay, alaska. *IEEE Geoscience and Remote Sensing Letters*, *10*(5), 1200–1204. https://doi.org/10.1109/LGRS.2012.2236075

Larson, K. M., Small, E. E., Gutmann, E., Bilich, A., Axelrad, P., & Braun, J. (2008). Using GPS multipath to measure soil moisture fluctuations: Initial results. *GPS solutions*, *12*, 173–177.

Lin, B., Katzberg, S. J., Garrison, J. L., & Wielicki, B. A. (1999). Relationship between GPS signals reflected from sea surfaces and surface winds: Modeling results and comparisons with aircraft measurements. *Journal of Geophysical Research: Oceans*, *104*(C9), 20713–20727.

Löfgren, J. S., & Haas, R. (2014). Sea level measurements using multi-frequency GPS and GLONASS observations. *EURASIP J. Adv. Signal Process.*, *2014*, 50.

Lomb, N. R. (1976). Least-squares frequency analysis of unequally spaced data. *Astrophysics and space science*, *39*, 447–462.

Madsen, S. N., & Zebker, H. A. (1998). Imaging radar interferometry. *Manual of remote sensing*, *2*, 349–380.

Martin et al. (2017). Radar-Interferometrie. *Lexikon der Geowissenschaften*.

Martin-Neira et al. (1993). A passive reflectometry and interferometry system (PARIS): Application to ocean altimetry. *ESA journal*, *17*(4), 331–355.

Nievinski, F. G., & Larson, K. M. (2014). Forward modeling of GPS multipath for near-surface reflectometry and positioning applications. *GPS solutions*, *18*, 309–322.

Pearce, J., & Mittleman, D. (2002). Defining the fresnel zone for broadband radiation. *Phys. Rev. E*, *66*, 056602. https://doi.org/10.1103/PhysRevE.66.056602

Por, E., van Kooten, M., & Sarkovic, V. (2019). Nyquist–Shannon sampling theorem. *Leiden University*, *1*(1).

Riecken, J., & Kurtenbach, E. (2017). Der Satellitenpositionierungsdienst der deutschen Landesvermessung–SAPOS®. (German) [the satellite positioning service of the surveying and mapping agencies of the laender of the federal republic of germany (adv)]. *ZfV-Zeitschrift für Geodäsie, Geoinformation und Landmanagement*, (zfv 5/2017).

Roesler, C., & Larson, K. M. (2018). Software tools for gnss interferometric reflectometry (gnss-ir). *GPS Solutions*, *22*(80). https://doi.org/10.1007/s10291-018-0744-8

Rosmorduc, V., Benveniste, J., Lauret, O., Maheu, C., Milagro, M., & Picot, N. (2011). Radar altimetry tutorial. *ESA, Europe*, 112–128.

Sauer, V. B., & Turnipseed, D. P. (2010). *Stage measurement at gaging stations* (Vol. 3). US Department of the Interior, US Geological Survey.

Scargle, J. D. (1982). Studies in astronomical time series analysis. II-Statistical aspects of spectral analysis of unevenly spaced data. *Astrophysical Journal, Part 1, vol. 263, Dec. 15, 1982, p. 835-853.*, *263*, 835–853.

Schüler, T. (2001). *On ground-based GPS tropospheric delay estimation* (Doctoral dissertation). Universtät der Bundeswehr Müchen, Universitätsbibliothek.

Strandberg, J., Hobiger, T., & Haas, R. (2016). Improving gnss-r sea level determination through inverse modeling of snr data. *Radio Science*, *51*(8), 1286–1296.

Strandberg, J., Hobiger, T., & Haas, R. (2017). Coastal sea ice detection using ground-based gnss-r. *IEEE geoscience and remote sensing letters*, *14*(9), 1552–1556.

SWR. (2023). Pegel, Wassertiefe, Wasserstand - das ist der Unterschied. (German) [gauge, waterdepth, water level - that's the difference] [[Online; Stand 15. Januar 2023]]. https://www.swr.de/swraktuell/rheinland-pfalz/was-ist-ein-pegel-erklaerung-100.html

VanderPlas, J. T. (2018). Understanding the Lomb-Scargle Periodogram. *The Astrophysical Journal Supplement Series*, *236*(1), 16. https://doi.org/10.3847/1538-4365/aab766

Wan, W., Larson, K. M., Small, E. E., Chew, C. C., & Braun, J. J. (2015). Using geodetic gps receivers to measure vegetation water content. *Gps Solutions*, *19*, 237–248.

Wasserstraßen- und Schiffsverwaltung des Bundes. (n.d.). Staustufe und Schleuse Iffezheim. (German) [barrage and sluice iffezheim]. https://www.wsa-oberrhein.wsv.de/Webs/WSA/Oberrhein/DE/1_Wasserstrasse/Bauwerke-und-Unterhaltung/Schleuse-Iffezheim/std_node.html

Wasserstraßen- und Schiffsverwaltung des Bundes. (1999). Der Wasserstand und Höhensysteme. (German) [water height and height system]. https://www.pegelonline.wsv.de/gast/hilfe#wasserstand

Wikipedia. (2023). Pegel — Wikipedia, die freie Enzyklopädie. (German) [gauge — wikipedia, the free encyclopedia [[Online; Stand 23. August 2023]]. https://de.wikipedia.org/wiki/Pegel#Begriffskl%C3%A4rung

Williams, S. (2023). GNSS-IR Water Levles, background on models and methods needed/used for water monitoring. https://morefunwithgps.com/public_html/Day3-Williams-backgroundWater.pdf

Williams, S., & Nievinski, F. (2017). Tropospheric delays in ground-based gnss multipath reflectometry—experimental evidence from coastal sites. *Journal of Geophysical Research: Solid Earth*, *122*(3), 2310–2327.

Wittmers, A., & Gensel, M. (2006). Modellierung von Kurven und Flächen mittels B-Splines. (German) [modeling of curves and surfaces using b-splines] [[Last Call: 07.12.2023]]. https://www.inf.fu-berlin.de/lehre/SS06/Computergraphik/skript/vorlesung4.pdf

Zavorotny, V. U., Gleason, S., Cardellach, E., & Camps, A. (2014). Tutorial on remote sensing using GNSS bistatic radar of opportunity. *IEEE Geoscience and Remote Sensing Magazine*, *2*(4), 8–45.

Zentrale Stelle SAPOS. (2023). Forschung und Entwicklung. (German) [research and developement] [[Online; Stand 5. September 2023]]. https://zentrale-stelle-sapos.de/forschung-entwicklung/